Geol. Mag. **155** (*5*), *2018, pp. 1150–1174.* © *Cambridge University Press 2017*
doi:10.1017/S0016756817000061

Origin and tectonic evolution of the NE basement of Oman: a window into the Neoproterozoic accretionary growth of India?

BRANDON L. ALESSIO*†, MORGAN L. BLADES*, GEORGE MURRAY*, BENJAMIN THORPE*, ALAN S. COLLINS*, DAVID E. KELSEY*, JOHN FODEN*, JUSTIN PAYNE‡, SALAH AL-KHIRBASH§ & FRED JOURDAN¶

*Centre for Tectonics, Resources and Exploration (TRaX), Department of Earth Sciences, The University of Adelaide, Adelaide, SA 5005, Australia
‡Centre for Tectonics, Resources and Exploration (TRaX), School of Built and Natural Environments, University of South Australia, Adelaide, SA 5095, Australia
§Sultan Qaboos University, Al Khoudh 123, Muscat, Oman
¶Western Australian Argon Facility, Curtin University, GPO Box U1987, Perth, WA 6845, Australia.

(*Received* 26 July 2016; *accepted* 30 January 2017; *first published online* 7 March 2017)

Abstract – The Omani basement is located spatially distant from the dominantly juvenile Arabian–Nubian Shield (ANS) to its west, and its relationship to the amalgamation of those arc terranes has yet to be properly constrained. The Jebel Ja'alan (NE Oman) basement inlier provides an excellent opportunity to better understand the Neoproterozoic tectonic geography of Oman and its relationship to the ANS. To understand the origin of this basement inlier, we present new radiogenic isotopic data from igneous bodies in Jebel Ja'alan. U–Pb and $^{40}Ar/^{39}Ar$ geochronological data are used to constrain the timing of magmatism and metamorphism in the jebel. Positive εHf and εNd values indicate a juvenile origin for the igneous lithologies. Phase equilibria modelling is used to constrain the metamorphic conditions recorded by basement. Pressure–temperature (*P–T*) pseudosections show that basement schists followed a clockwise *P–T* path, reaching peak metamorphic conditions of *c.* 650–700 °C at 4–7.5 kbar, corresponding to a thermal gradient of *c.* 90–160 °C/kbar. From the calculated thermal gradient, in conjunction with collected trace-element data, we interpret that the Jebel Ja'alan basement formed in an arc environment. Geochronological data indicate that this juvenile arc formed during Tonian time and is older than basement further west in Oman. We argue that the difference in timing is related to westwards arc accretion and migration, which implies that the Omani basement represents its own tectonic domain separate to the ANS and may be the leading edge of the Neoproterozoic accretionary margin of India.

Keywords: Jebel Ja'alan, U–Pb geochronology, thermochronology, pseudosection, palaeogeography.

1. Introduction

The Sultanate of Oman is host to a number of discrete exposures of basement rock that preserve complex histories that include a number of magmatic, metamorphic and deformational events (Gass *et al.* 1990; Mercolli *et al.* 2006; Rantakokko *et al.* 2014; Whitehouse, Pease & Al Khirbash, 2016). These exposures offer an insight into the palaeogeography of the region during Neoproterozoic time, a period of severe glacial episodes and the radiation of the Ediacaran fauna (e.g. Hoffman *et al.* 1998; Meert & Lieberman, 2008; Halverson *et al.* 2009). A number of authors have used geochemistry to interpret the tectonic setting of the igneous and metamorphic basement of Oman to suggest that it formed in an intra-oceanic volcanic-arc setting (Gass *et al.* 1990; Mercolli *et al.* 2006; Bowring *et al.* 2007; Rieu *et al.* 2007; Rantakokko *et al.* 2014) within the Neoproterozoic Mozambique Ocean (Johnson & Woldehaimanot, 2003; Kröner & Stern, 2004; Allen, 2007; Bowring *et al.* 2007; Rantakokko *et al.* 2014). The relationship between the Omani basement and the arc terranes of the Arabian–Nubian Shield (ANS) has been addressed by several authors, but with little consensus as to whether it should be considered an eastern extension of the ANS (Johnson & Woldehaimanot, 2003; Collins & Pisarevsky, 2005; Johnson *et al.* 2011; Rantakokko *et al.* 2014; Whitehouse, Pease & Al Khirbash, 2016; Merdith *et al.* in press).

Jebel Ja'alan lies in eastern Oman (Fig. 1) and contains well-exposed metamorphic and igneous rocks that comprise a rare window into the basement of far eastern Arabia. The area is of considerable significance because, within Gondwana, eastern Arabia sits within a poorly known region that separates the well-exposed Arabian Shield from Rajasthan in NW India (Collins & Pisarevsky, 2005). Eastern Arabia is almost entirely covered by Phanerozoic rocks, with occurrences of Neoproterozoic outcrop being small and limited in number. In this context, Jebel Ja'alan's rocks preserve evidence for the Neoproterozoic tectonic geography between Neoproterozoic India and the ANS.

In this study we present U–Pb (monazite and zircon) and $^{40}Ar/^{39}Ar$ (muscovite) geochronological data

---

†Author for correspondence: brandon.alessio@adelaide.edu.au

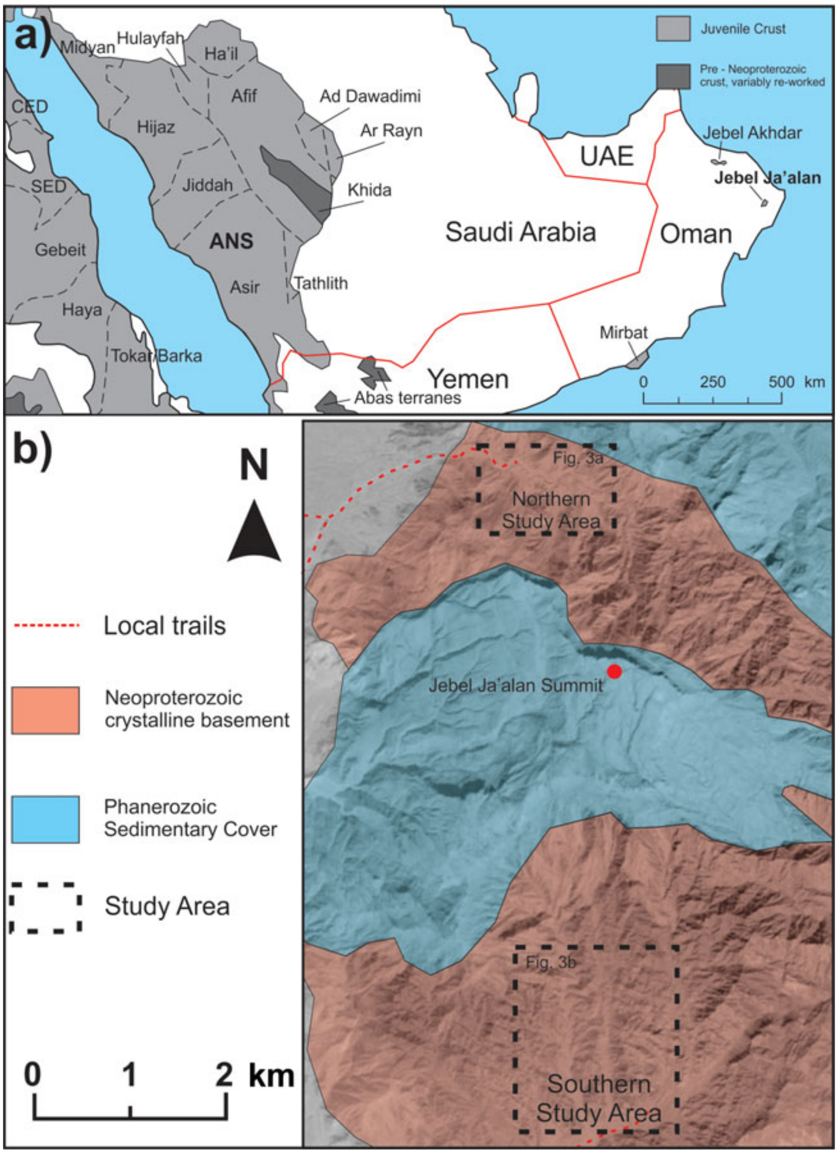

Figure 1. (Colour online) (a) Location map of the Arabian–Nubian Shield (ANS) and Oman (adapted from Blades *et al.* 2015; Allen, 2007). Note the >800 km gap between the basement exposed in Oman and the nearest terranes of the ANS. (b) Location map of Jebel Ja'alan; study areas are indicated by the black dashed boxes.

in order to constrain the timing of crystallization of igneous intrusions in the Jebel Ja'alan region, as well as the timing of metamorphism of the country rocks. Radiogenic isotopic data (Hf, Nd) from igneous bodies in Jebel Ja'alan are used to interpret the origin of the basement, whereas phase equilibria modelling in conjunction with trace-element geochemical data from igneous rocks are used to constrain the tectonic setting in which these rocks formed. The results of this study are used to argue that the basement of Jebel Ja'alan indeed formed in a juvenile volcanic-arc environment during Tonian time, but with resolvable differences to other exposures of Omani basement. These conclusions are similar to those from a recent study by Whitehouse, Pease & Al Khirbash (2016), who investigated the same area with a more restrictive dataset. We also discuss the regional significance of these results and observations and argue that the Omani basement represents its own tectonic domain separate to the ANS and more related to NW India, Pakistan, the Seychelles and the Bemarivo Belt of north Madagascar.

2. Geological setting

2.a. Oman and the Arabian–Nubian Shield (ANS)

Numerous authors have recognized the similarities between the basement rocks of Oman and those of Yemen and the ANS. Many note the possibility that Oman represents an eastern extension of the ANS (Gass *et al.* 1990; Immenhauser *et al.* 2000; Collins & Pisarevsky, 2005; Worthing, 2005; Stern & Johnson, 2010; Rantakokko *et al.* 2014), which was described by Johnson *et al.* (2011) as a collage of Neoproterozoic juvenile arcs, younger sedimentary and volcanic basins, granitoid intrusions and enclaves of pre-Neoproterozoic crust. However, the absence of pre-Phanerozoic outcrop between Oman and the Arabian Shield of Saudi Arabia impede any direct connection between the regions (Johnson & Woldehaimanot, 2003; Collins & Pisarevsky, 2005; Rantakokko *et al.* 2014). Crustal growth of the ANS is commonly interpreted to have occurred during *c*. 870–600 Ma (Johnson & Woldehaimanot, 2003; Meert, 2003; Kröner & Stern, 2004; Stern & Johnson, 2010), with volcanic arcs formed on the juvenile crust of the Mozambique Ocean (Johnson & Woldehaimanot, 2003; Meert, 2003; Kröner & Stern, 2004; Rantakokko *et al.* 2014). However, reports of Stenian (1030–1020 Ma) volcanic-arc rocks in the Sinai (Be'eri-Shlevin *et al.* 2012) hint at a pre-Neoproterozoic origin for subduction in the region that questions the long-held view of an early Tonian rift history forming the Mozambique Ocean (Stern, 1994).

Amalgamation of these arc terranes and associated ophiolitic remnants, which form the majority of the exposed ANS, are interpreted to have occurred as early as *c*. 845 Ma (Robinson *et al.* 2014; Robinson, Foden & Collins, 2015*a*) via arc–arc convergence and terrane suturing (Johnson & Woldehaimanot, 2003; Robinson *et al.* 2014; Robinson, Foden & Collins, 2015*a*). Several studies note that the youngest exposed volcanic-arc magmatism and arc accretion occur in the easternmost exposed part of the ANS (Doebrich *et al.* 2007; Johnson *et al.* 2011; Cox *et al.* 2012), which suggests that younger arc terranes may lie beneath the Rub Al-Khali basin where magnetic highs similar to the ANS arcs occur (Johnson & Stewart, 1995). The terranes that comprise the western ANS were recently shown to have accreted to the East Saharan Craton during Cryogenian time (Westerhof *et al.* 2014; Blades *et al.* 2015), but the central terranes – that may have earlier amalgamated into a discrete ANS continent – are thought to have accreted onto the East Saharan Craton during late Cryogenian–Ediacaran time (Meert, 2003; Li *et al.* 2008; Johnson *et al.* 2011). This suggests that arc volcanism and accretion in the ANS continued to occur long after similar processes had ceased in Oman around early Cryogenian time (Mercolli *et al.* 2006; Rantakokko *et al.* 2014). During late Neoproterozoic time, volcanic-arc-related processes in Oman were superseded by deposition of the Huqf Supergroup (Leather *et al.* 2002; Allen, Leather & Brasier, 2004; Allen, 2007; Bowring *et al.* 2007; Rieu *et al.* 2007; Allen *et al.* 2011). The strata of the Huqf Supergroup contain glacial deposits and cap-carbonates overlain by siliciclastic and carbonate shelf deposits, which are in turn overlain by evaporites, carbonates and organic-rich shales (Leather *et al.* 2002; Allen, Leather & Brasier, 2004; Allen, 2007; Bowring *et al.* 2007; Rieu *et al.* 2007; Allen *et al.* 2011). Allen (2007) suggests that the sedimentary sequences seen in the Huqf Supergroup represent a rift sequence, followed by a passive margin succession. Rieu *et al.* (2007) suggests that these correlate with similar successions exposed in the Salt Range of Pakistan and in the Bikaner–Nagaur Basin that straddles the border of India and Pakistan.

2.b. Jebel Ja'alan

Jebel Ja'alan is located in NE Oman, approximately 50 km south of the town of Sur (Fig. 1). The basement rocks exposed around the jebel have previously been dated as Neoproterozoic (Gass *et al.* 1990). These basement lithologies are unconformably overlain by chert conglomerates, lithic sandstones and shales or marls of the upper Campanian – lower Maastrichtian Qahlah Formation, whereas the summit is capped by conformably overlying Maastrichtian limestones of the Simsima Formation (Filbrandt, Nolan & Ries, 1990). On the northern side of the inlier are metapelitic schist and orthogneiss, with rarer occurrences of variably deformed granodiorite, granite, diorite and hornblendite (Gass *et al.* 1990). On the southern side of the mountain lies an extensive undeformed granite pluton that intrudes the schist and gneiss that crop out to the north. The granite pluton is cross-cut by several distinct dyke generations of varying chemistry and orientation. The granite was previously dated by Pallister *et al.* (1990), who published U–Pb ages of granite intrusions in Jebel Ja'alan ranging over 830–825 Ma. Gass *et al.* (1990) published a Rb–Sr whole-rock isochron age for the Ja'alan Granite of 850 ± 27 Ma. These authors also reported a Rb–Sr isochron age of 773 ± 34 Ma for the orthogneiss and a K–Ar whole-rock age of 430 ± 20 Ma for a mafic dyke, although the significance of those apparent whole-rock ages is questionable due to these rocks likely being at least partially altered. A more recent study by Whitehouse, Pease & Al Khirbash (2016) produced SIMS U–Pb zircon crystallization ages for the Ja'alan Granite and Ja'alan Gneiss, ranging over 840–825 Ma and 900–880 Ma, respectively. These authors also obtained Nd isotopic data for these lithologies, which gave juvenile εNd(t) values ranging from +6 to +1.5. This is suggested to correspond to increased crustal contamination relative to the Mirbat region, reflecting successive outwards growth from a continental margin.

3. Methodology

Samples were collected from various lithologies found within the Jebel Ja'alan area. These were analysed for geochronology, geochemistry and thermobarometric forward modelling as detailed below. The structural context of these samples was constrained by mapping an approximate 2×3.5 km area of the region, which is fully described in the online supplementary material (available at http://journals.cambridge.org/geo). Lower-hemisphere equal-area stereographic projections were created for structural data using the Stereonet 9 program, based on algorithms described by Cardozo & Allmendinger (2013) and Allmendinger, Cardozo & Fisher (2011).

3.a. Geochronology and isotope geochemistry

3.a.1. U–Pb monazite and zircon

Zircon was analysed to constrain magmatic crystallization ages whereas monazite was analysed to constrain the age of metamorphism. U–Pb age data were obtained from *in situ* monazite grains as well as separated zircon grains that were extracted from crushed rocks using standard magnetic and heavy liquid techniques. Zircon separates were hand-picked, mounted in epoxy resin and then polished to expose the grains. The thin-sections and grains were imaged on Phillips XL30 and XL20 scanning electron microscopes (SEM), respectively. Zircon grains were imaged using a cathodoluminescence (CL) detector to identify internal structure prior to isotopic analysis. Zircon and monazite grains were analysed via laser ablation inductively coupled plasma mass spectrometry (LA–ICP–MS), using an Agilent 7500cs and NewWave UP213 laser ablation system. Imaging of grains and measuring of U–Pb isotopes was conducted at Adelaide Microscopy, located at the University of Adelaide. Ablation of monazite and zircon was performed in a He-ablation atmosphere with a frequency of 5 Hz. A spot size of 10 μm was used for all monazite samples and 30 μm for all zircon samples. The acquisition time for all monazite samples was 80 s in total, with 30 s of background acquisition, 10 s of the laser firing with the shutter closed to ensure beam stabilization and 40 s of sample ablation. Zircon samples had an acquisition time of 60 s total, with 30 s of background acquisition followed by 30 s of sample ablation. Elemental fractionation and mass bias for monazite grain analyses were corrected using the primary standard MAdel (^{207}Pb/^{206}Pb $= 491 \pm 2.7$ Ma, ^{206}Pb/^{238}U $= 518.37 \pm 0.99$ Ma, ^{207}Pb/^{235}U $= 513.13 \pm 0.19$ Ma; Payne *et al.* 2008). Data accuracy was monitored using the monazite standard 94–222/Bruna-NW (*c.* 450 Ma; Payne *et al.* 2008). Throughout this study MAdel yielded weighted mean ages of ^{207}Pb/^{206}Pb $= 492 \pm 14$ Ma, ^{206}Pb/^{238}U $= 518 \pm 5.2$ Ma, ^{207}Pb/^{235}U $= 513 \pm 4.8$ Ma ($n = 29$, 2σ errors). The zircon standard (GJ) (^{206}Pb/^{238}U $= 608.5 \pm 0.4$ Ma; Jackson *et al.* 2004) was used as the primary standard for all zircon analyses, while Plešovice (^{206}Pb/^{238}U $= 337.13 \pm 0.37$ Ma; Sláma *et al.* 2008) was used as a secondary standard. Throughout this study Plešovice yielded an average ^{206}Pb/^{238}U age of 333.8 ± 2.1 Ma ($n = 80$, 2σ errors). U–Pb data were reduced using Gemoc laser ICPMS total trace-element reduction (GLITTER; Jackson *et al.* 2004).

3.a.2. Lu–Hf

An ESI New Wave UP-193 nm excimer laser attached to a Thermo-Scientific Neptune Multi-Collector ICP–MS at The University of Adelaide was used to measure the concentration of Hf isotopes in zircon grains. Analytical methods follow Payne *et al.* (2013) and Griffin *et al.* (2002). A spot size of 50 μm was used for all appropriately sized zircon grains, decreasing to 25 μm when required. Zircons were ablated in a helium atmosphere, which was mixed with argon upstream of the ablation cell, for 40–100 s with a 5 Hz repetition rate, a 4 ns pulse rate and an intensity of 10 J cm^{-2}. Known standards were run before and between the unknown samples to verify the stability and performance of the instrument. The primary standard used was Plešovice, which yielded a mean ^{176}Hf/^{177}Hf ratio of 0.282470 ± 0.000015. This compares to the published value of 0.282482 ± 0.000013 provided by Sláma *et al.* (2008). During the study Plešovice also yielded a mean ^{178}Hf/^{177}Hf ratio of 1.46730 ± 0.00028, which is also in agreement with that published (1.46723 ± 0.00002 and 1.46719 ± 0.00010) by Sláma *et al.* (2008). Reduction of zircon data was undertaken using the Hf isotope data reduction spreadsheet, HfTRAX (Payne *et al.* 2013). Data were normalized to ^{179}Hf/^{177}Hf $=$ 0.7325, using an exponential correction for mass bias. Yb and Lu isobaric interferences on ^{176}Hf were corrected for following the methodology of Woodhead *et al.* (2004).

3.a.3. ^{40}Ar/^{39}Ar

Two samples of muscovite were used for ^{40}Ar/^{39}Ar dating. Grains were separated using a paper-shaking technique then hand-picked and sent to the Western Australia Argon Isotope Facility, Curtin University. Samples were loaded into wells and bracketed by small wells that included Fish Canyon sanidine (FCs) used as a neutron monitor yielding an age of 28.294 ± 0.13 Ma (1σ) using the decay constants proposed by Renne *et al.* (2011). The correction factors for interfering isotopes were (^{39}Ar/^{37}Ar)Ca $= 7.30 \times 10^{-4}$ (± 11 %), (^{36}Ar/^{37}Ar)Ca $= 2.82 \times 10^{-4}$ (± 1 %) and (^{40}Ar/^{39}Ar)K $= 6.76 \times 10^{-4}$ (± 32 %). Samples were step-heated using a 110 W Spectron laser system, with a continuous Nd–YAG (IR: 1064 nm) laser. Ar isotopes were measured in static mode using a MAP 215–50 mass spectrometer, with a Balzers SEV 217 electron multiplier primarily using nine to ten cycles of peak-hopping.

3.a.4. Samarium–neodymium, rubidium–strontium isotopes

Isotopic analyses of Sm, Nd and Sr were conducted on samples of the igneous lithologies located in southern Jebel Ja'alan. Preparation and analysis of whole-rock isotopic data follow procedures implemented by Payne *et al.* (2008) and Wade *et al.* (2008). Isotopic ratios were measured on a Finnigan MAT262 thermal ionization mass spectrometer (TIMS). The neodymium standard JDNi-1 returned a mean ^{143}Nd/^{144}Nd value of 0.512074 ± 0.00001 ($n = 5$). The blanks show negligible Nd and Sm. When calculating εNd values an approximated age of 840 Ma was used, as this is the interpreted crystallization age (Gass *et al.* 1990).

3.b. Elemental geochemistry

3.b.1. Whole-rock geochemistry

Whole-rock geochemical analysis of Al Wafi Mica Schist sample JA15-04 for phase equilibria forward modelling of two schist samples was undertaken using X-ray fluorescence (XRF) at Bureau Veritas Minerals (Western Australia). Major elements were analysed on fused beads using a lithium tetraborate flux, as described by Kil & Jung (2015). All other samples were geochemically analysed via XRF at a CSIRO laboratory (South Australia). Trace-element analysis was carried out using LA–ICP–MS. These analyses used fused XRF disks prepared using the methodology outlined by Kil & Jung (2015).

3.b.2. Mineral chemistry

Chemical compositions of silicate minerals used to constrain *P*–*T* conditions were obtained via electron probe micro-analysis (EPMA) using a CAMECA SX5 microprobe at the University of Adelaide. A beam current of 20 nA and an accelerating voltage of 15 kV were used for all point analyses.

3.b.3. Phase equilibria forward modelling

Pseudosections were calculated for Al Wafi Mica Schist samples (JA15-04 and JA15-43) using the bulk composition obtained for sample JA15-04 via XRF analysis. The bulk composition of JA15-04 is argued to be a valid proxy for JA15-43, due to their similarity in both preserved mineral assemblage and measured mineral compositions (refer to supplementary material). Pseudosections were calculated using the phase equilibrium modelling program ThermoCalc v.3.37 with the internally consistent thermodynamic dataset of Holland & Powell (2011), ds62. Quantitative *P*–*T* information was calculated for the geologically realistic system MnNCKFMASHTO ($MnO–Na_2O–CaO–K_2O–FeO–MgO–Al_2O_3–SiO_2–H_2O–TiO_2–Fe_2O_3$). Activity–composition (*a*–*X*) models used are from Powell *et al.* (2014), White *et al.* (2014) and White, Powell & Johnson (2014). Numerous authors highlight the uncertainty of H_2O and Fe_2O_3 abundances measured during routine whole-rock geochemical (XRF) analyses (Fitton & Gill, 1970; Korhonen, Powell & Stout, 2012; Kelsey & Hand, 2015; Morrissey, Hand & Kelsey, 2015). As such, appropriate H_2O and Fe_2O_3 ('O') contents for each modelled sample were evaluated via the calculation of T–M_{H2O} and T–M_O pseudosections prior to the calculation of *P*–*T* pseudosections.

4. Results

4.a. Field-based geology

4.a.1. Lithological units

In the field, ten distinct lithologies were encountered: metapelitic schist (Al Wafi Mica Schist; Roger *et al.* 1991; referred to here as the Al Wafi Schist), orthogneiss (Ja'alan Gneiss; Roger *et al.* 1991), titanite-biotite-sillimanite-staurolite ± muscovite schist, granite (Ja'alan Granite, equivalent to the Ja'alan batholith of Roger *et al.* 1991), granodiorite (Kamil Granodiorite), dolerite dykes (informally divided into the 'Brown Dolerite' and 'Grey Dolerite' based on their weathering colour), andesite dykes, hornblendite and sedimentary rocks of the Qahlah Formation. These lithologies are summarized in Table 1. Cross-cutting relationships suggest that the 'Grey Dolerite' is the oldest dyke generation, succeeded by the andesite then 'Brown Dolerite' dykes. Magma mingling textures observed between the 'Grey Dolerite'/andesite dykes and the Ja'alan granite indicate that these dykes likely intruded prior to cooling of the granite. Photographs of the dominant lithologies and key cross-cutting relationships are presented in Figure 2. Detailed descriptions of the mapped lithologies are provided in the supplementary material.

4.a.2. Rock relations and structural geology

Structural and lithological data from the north and south study areas of Jebel Ja'alan are presented in Figure 3. Al Wafi Schist and Ja'alan Gneiss dominate the region to the north of Jebel Ja'alan. The Al Wafi Schist occurs in the west of the study area and has a structural contact with the SE Ja'alan Gneiss. To the east, the Ja'alan Gneiss is thrust top-to-the-north over the Al Wafi Schist along a broadly E–W-aligned boundary, whereas the western boundary of the Ja'alan Gneiss is marked by a N–S-striking, top-to-the-east thrust of Al Wafi Schist over the Ja'alan Gneiss.

The foliation data (S_1; Fig. 3a, stereonets iii and iv) indicate two phases of folding. The first phase of folding (F_1) is interpreted from a series of approximately ENE-trending folds. The second phase (F_2) is interpreted from a pair of approximately N–S-trending folds that overprint the earlier folds and fold the Ja'alan Gneiss over Al Wafi Schist thrust. Measurements of minor fold axial planes from the Ja'alan Gneiss (Fig. 3a, stereonets ii and vi) are broadly E–W striking and are consistent with the first phase of folding. However, N–S-striking axial planes from the Al Wafi Schist are interpreted as being related to this second phase of N–S-trending folding. Mineral aggregate lineation data (Fig. 3a, stereonets i and v) from both lithologies correlate reasonably well with the plunge and plunge direction of the fold hinges calculated from foliation measurements (12→237 for the Al Wafi Schist, 08→230 for the Ja'alan Gneiss), but can be seen to consistently trend in a more southerly direction (*c.* 200°). The folding of this contact and supra-position of N–S-trending folds over earlier, broadly E–W-trending folds suggests that a N–S contraction (D_1) pre-dated an E–W contraction (D_2). The N–S folds interpreted as forming in the same stress field as the N–S striking thrust and the E–W trending folds are interpreted with the same stress field that

Table 1. Summary and description of lithologies encountered in the Jebel Ja'alan study areas (bi – biotite; chl – chlorite; cpx – clinopyroxene; ep – epidote; grt – garnet; hbl – hornblende; ilm – ilmenite; kfs – K-feldspar; ms – muscovite; mt – magnetite; pl – plagioclase; py – pyrite; qtz – quartz; sil – sillimanite; st – staurolite; ttn – titanite).

Lithological unit	Mineralogy	Textural and structural features	Additional characteristics
Qahlah Formation (Filbrandt, Nolan & Ries, 1990)	Unfossiliferous interbedded red or yellow pebbly chert conglomerates, lithic sandstones and shales or marls of fluvial origin.	Bioturbated marine facies are present at the top of the sequence.	Conformably overlain by Maastrichtian limestones of the Simsima Formation. Observed to unconformably overlie basement rock in the SW and NE corners of the northern mapping area.
Chl-Pl-Cpx 'Brown' Dolerite	Fine- to medium-grained (0.2–1 mm) pl-cpx-chl.	Cpx and pl grains are significantly deformed, with few cpx grains displaying a distinct crystal form. Pericline twinning exhibited in several pl grains. Weathers to a brown colour.	Occurs as final generation of dykes that cross-cut all other basement lithologies in Jebel Ja'alan region.
Andesite	Fine- to coarse-grained (0.3–3 mm) crowded pl-rich assemblage, hbl replacing chl and ttn. Mt-ep as accessories.	Coarser grained than other dyke generations, similar dip angle to the grey dolerite.	Similar dip angle to the grey dolerite suggests they are part of the same suite.
Pl-Hbl 'Grey' Dolerite	Fine- to medium-grained (0.2–1 mm) pl ± qtz and kfs groundmass, hbl-ep-bi.	Glomeroporphyritic texture of plagioclase phenocrysts. Cracks in the dolerite are often filled with granite. Weathers to a grey colour.	First generation of dykes. Many of these dykes display magma mingling at their margins where an intermediate rock had crystallized between it and the Ja'alan Granite.
Ttn-Bi-Sil-St ± Ms Schist	Coarse (1–2 mm) pl-qtz with medium to fine (0.2–1) pl-qtz-st-sil-bt-ttn and minor py-ms.	Pervasive reaction textures present throughout rock showing features indicating breakdown of pl and bt. Ttn grains abundant throughout rock as well-defined and relatively undeformed crystals.	Localized to south of the northern mapping area, where it is observed as a single outcrop within the Ja'alan Gneiss.
Kamil Granodiorite	Coarse-grained (1–3 mm) qtz-grt-pl with finer (<0.75 mm) bt-kfs. Coarser (3–5 mm) grt phenocrysts are observed in a relatively finer qtz-pl-kfs-bt groundmass.	Coarse overall texture with finer bt and kfs. Reaction texture throughout rock showing the breakdown of pl. Varying degrees of deformation within grt phenocrysts.	Found as small intrusions within the Al Wafi Schist in the northern within the northern field area, often bordering the Ja'alan Gneiss. Observed as small intrusions within the Ja'alan granite in the southern field area.
Hornblendite	Coarse (1–4 mm) hbl (60–70 %)-cpx-pl with minor bi.	Reaction texture present indicating breakdown of pl.	Restricted to two outcrops observed within the Ja'alan Gneiss in the south and east of the north mapping area. Observed extensively within Ja'alan Granite in the SE portion of the southern field area. Ambiguous field relationship.
Ja'alan Granite	Coarse (1–2 mm) qtz-pl-kfs-ms-grt.	Coarse, granoblastic texture.	Found dispersed within the Jebel Ja'alan area as bodies of various size. Intrude both the Al Wafi Schist and Ja'alan Gneiss.
Al Wafi Schist	Fine-grained (<0.75 mm) qtz-pl-bi-ms-sil-ilm-mt-chl ± st ± grt with occurrences of coarse-grained (1–2 mm) qtz and pl. Peak assemblage qtz-pl-ms-sil-bi-ilm-mt ± grt ± st.	Fabric defined by bt-ms-sil with an aggregate mineral lineation defined by bt. Schistose foliation present throughout rock with partial melting observed in small areas. Breakdown of muscovite is interpreted from thin-section samples.	Metapelitic unit which occupies a large portion of the north and western mapping area. Inferred to thrust over the Ja'alan Gneiss along the N–S boundary between the units.
Ja'alan Gneiss	Fine- to medium-grained (0.3–1 mm) bt-ms-qtz-pl-sil-ilm-kfs with medium-to coarse-grained (0.7–3 mm) qtz.	Fabric defined by bt and ms, with an aggregate mineral lineation defined by bt. Gneissic foliation throughout rock with partial melting observed in small areas. Breakdown of muscovite is interpreted from thin-section samples.	Occupies a large portion of the northern study area. Observed to thrust over the Al Wafi Schist along the E–W boundary between the units. Borders the Ja'alan Granite batholith in the southern study area.

formed the thrust that juxtaposed the Ja'alan Gneiss over the Al Wafi Schist.

The Ja'alan Granite forms a batholith that dominates the area to the south of Jebel Ja'alan. The northern margin of the batholith forms an intrusive contact with the Ja'alan Gneiss, whereas to the SE it is bordered by a hornblendite that may be a co-magmatic cumulate. Dykes cross-cut all rocks and form three main swarms, identified on the basis of lithology, orientation and cross-cutting relationships. Early 'Grey Dolerite'

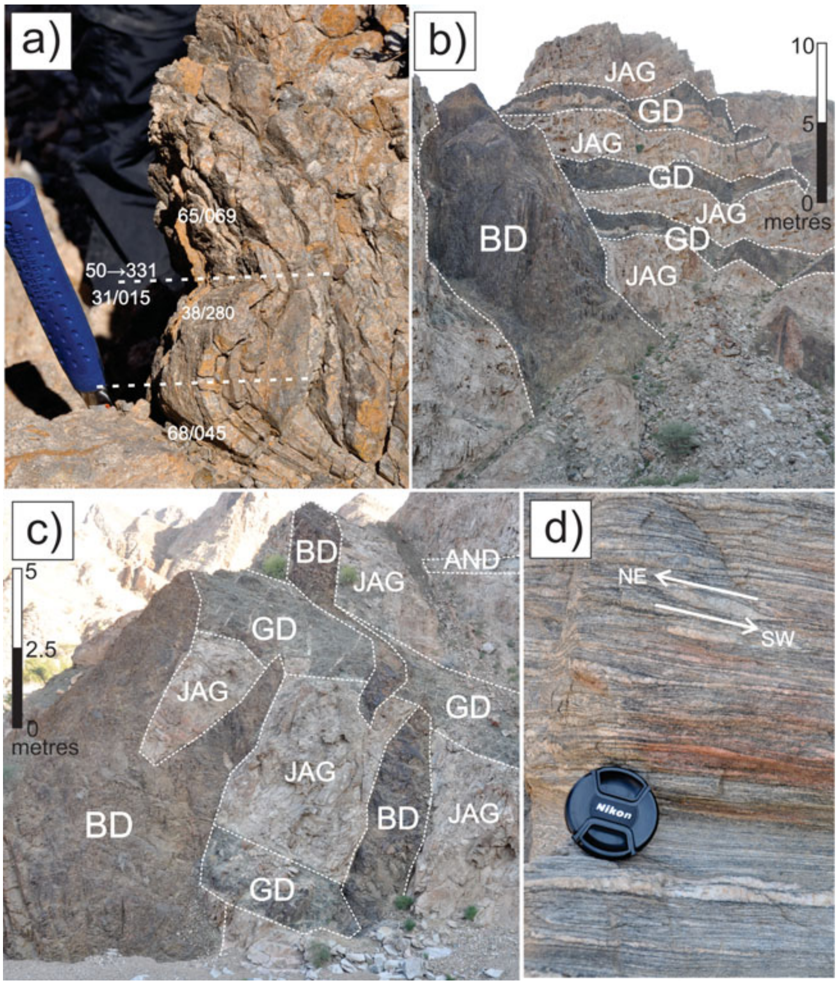

Figure 2. (Colour online) Field photos from Jebel Ja'alan. (a) Parasitic folding of the Al Wafi Schist with minor fold limb, axial plane and hinge measurements displayed. (b) Hill displaying the cross-cutting relationships between the Ja'alan Granite, Grey Dolerite and Brown Dolerite. (c) Outcrop again displaying the cross-cutting relationships between the Ja'alan Granite, Grey Dolerite and Brown Dolerite, but also showing the cross-cutting relationship between andesite dykes and the Ja'alan Granite. (d) Ja'alan Gneiss outcrop displaying a sigma clast that is indicative of a top-to-the-NE sense of movement.

and andesite dykes share similar dip angles and are interpreted to belong to the same suite. The orientation of these vary, but are commonly shallow dipping, have irregular margins, commonly mingle with the surrounding granite (Fig. 2c) and follow a rough NE–SW-aligned trend. A later suite of brown-weathering dolerite dykes cross-cut all other lithologies (the 'Brown Dolerite'). These are steeply dipping, easily visible on aerial imagery and consistently strike towards *c.* 120°.

4.b. U–Pb geochronology

LA–ICP–MS analytical data are presented in the supplementary material. Analyses have been categorized into their broadly identified internal structure based on SEM CL imaging and grains used for concordia age calculations. Data are presented using Wetherill concordia diagrams (^{207}Pb/^{235}U v. ^{206}Pb/^{238}U). All age uncertainties are quoted at the two sigma level. An attempt was made to analyse zircons from the Ja'alan Granite Batholith; the obtained data are however poor and full of common Pb, so have not been presented.

4.b.1. *Kamil Granodiorite*

Zircons in samples JA15-08 (742 899 m E, 2 460 099 m N) and JA15-09 (742 927 m E, 2 460 090 m N) (WGS84 reference frame, UTM coordinates, zone 40N) are usually clear with a slight yellow tint, with some grains being noticeably darker. Crystal lengths range from *c.* 50 μm to 250 μm, with aspect ratios generally being elongate prismatic (4:1) or occasionally stubby (1:1). CL images (Fig. 4) of all zircon grains showed oscillatory zonation, confirming an igneous origin (Corfu *et al.* 2003). Consequently, all analyses were targeted at the oscillatory-zoned zircon cores. Fifty U–Pb analyses were conducted on zircons separated from sample JA15-08 (Fig. 5). Forty analyses occur within 95 % of concordance and yielded ^{206}Pb/^{238}U single grain ages ranging over *c.* 970–760 Ma. The mean ^{206}Pb/^{238}U age was calculated to be 835 ± 9 Ma with a mean square weighted deviation (MSWD) of 5.8 ($n = 40$). Such an MSWD is too high for the number of zircon analyses undertaken and represents an over-dispersion in the data (Wendt & Carl, 1991). By examining the data in a weighted

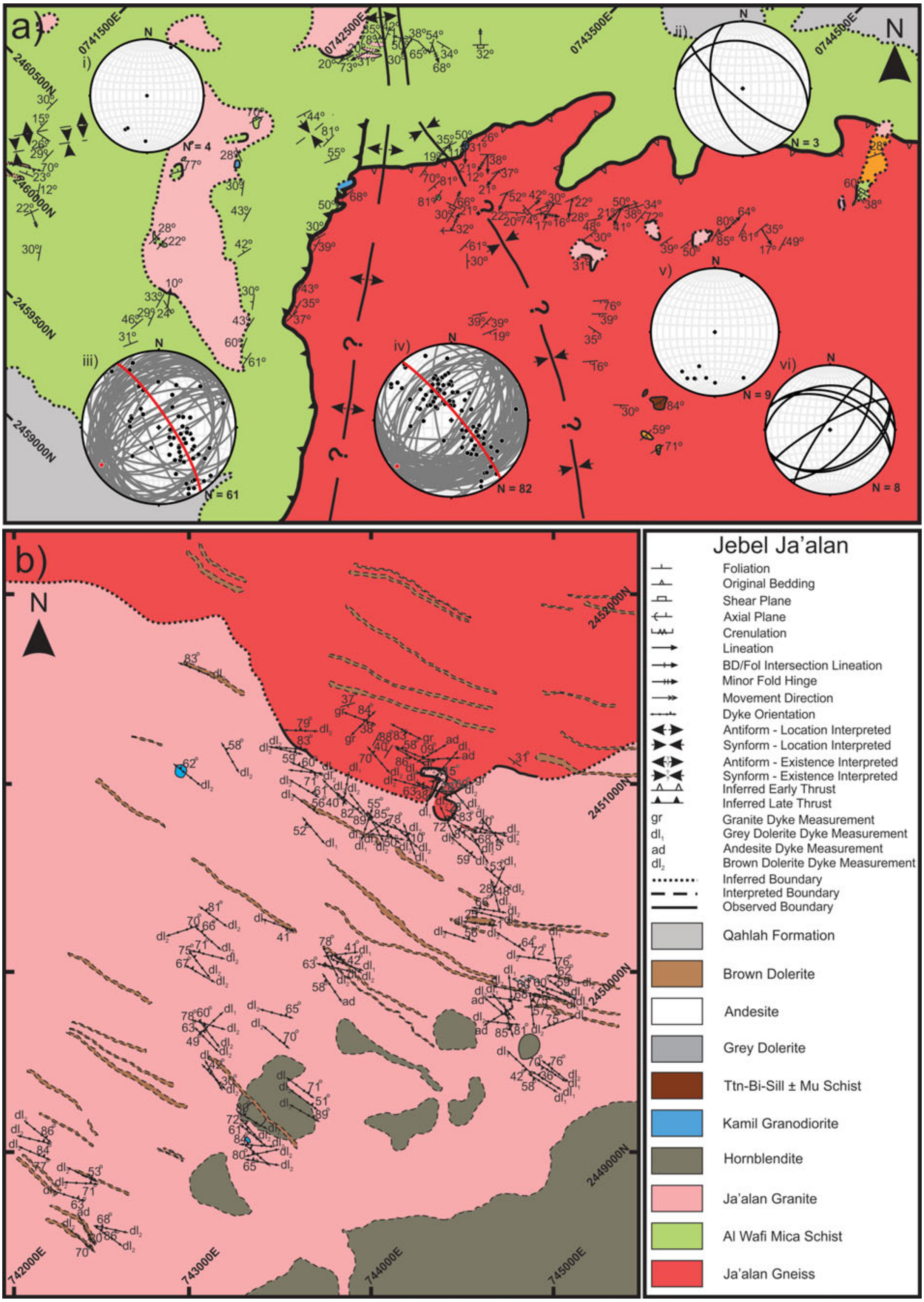
a)
b)
N
0741500E
0742500E
0743500E
0744500E
2460500N
2460000N
2459500N
2459000N
i)
N = 4
ii)
N = 3
iii)
N = 61
iv)
N = 82
v)
N = 9
vi)
N = 8
742000E
743000E
744000E
745000E
2452000N
2451000N
2450000N
2449000N
Jebel Ja'alan
Foliation
Original Bedding
Shear Plane
Axial Plane
Crenulation
Lineation
BD/Fol Intersection Lineation
Minor Fold Hinge
Movement Direction
Dyke Orientation
Antiform - Location Interpreted
Synform - Location Interpreted
Antiform - Existence Interpreted
Synform - Existence Interpreted
Inferred Early Thrust
Inferred Late Thrust
gr Granite Dyke Measurement
dl1 Grey Dolerite Dyke Measurement
ad Andesite Dyke Measurement
dl2 Brown Dolerite Dyke Measurement
Inferred Boundary
Interpreted Boundary
Observed Boundary
Qahlah Formation
Brown Dolerite
Andesite
Grey Dolerite
Ttn-Bi-Sill ± Mu Schist
Kamil Granodiorite
Hornblendite
Ja'alan Granite
Al Wafi Mica Schist
Ja'alan Gneiss

average plot (Fig. 5b), the four oldest grains were excluded from age calculations on the basis that they may represent inherited zircon. The youngest four zircons were also excluded on the interpretation that these grains may have been subjected to radiogenic Pb loss. Calculating a ^{206}Pb/^{238}U weighted average age with these grains excluded results in an age of 836 ± 4 Ma with an MSWD of 0.90 and P-value of 0.62 (n = 31), which is interpreted as a reliable estimate of the age of crystallization.

Forty-nine analyses were conducted on zircons from sample JA15-09 (Fig. 6). Of these analyses 32 grains occur with 95 % of concordance and yielded ^{206}Pb/^{238}U ages ranging over *c.* 897–802 Ma. A weighted average of these analyses yielded a ^{206}Pb/^{238}U age of 839 ± 7 Ma with an MSWD of 3.2 (n =32), again showing that the data do not belong to a single population. Further inspection of the data in a weighted average plot (Fig. 6b) led to the exclusion of the four noticeably oldest grains, which are interpreted as inherited. The fourth oldest grain could arguably be included in further age calculations as it produces a weighted average age with P-value >0.05, although we have excluded the analysis as it would be outside the error of the age it is used to produce. The youngest two grains were excluded on the basis that they may have experienced radiogenic Pb loss. A weighted average of the remaining analyses revealed an age of 836 ± 4 Ma with an MSWD of 1.10 and P-value of 0.33 (n = 26). This rounded age is the same as that calculated for JA15-08, and is interpreted to represent the age of crystallization of this sample.

4.b.2. *Ja'alan Gneiss*

Zircons from sample JA15-26 (743 437 m E, 2 459 614 m N) and JA15-36 (743 707 m E, 2 459 687 m N) (WGS84 reference frame, UTM coordinates, zone 40N) have a brown–yellow hue, with crystal lengths ranging from *c.* 50 μm to 180 μm. Aspect ratios of zircon grains range from equant (1:1) to elongate prismatic (4:1). Regardless of size and shape, zircons grains in this sample generally display oscillatory zonation typical of an igneous protolith (Fig. 4). U–Pb zircon analyses were conducted on 49 zircons from JA15-26, with 43 of these analyses being ≥95 % concordant (Fig. 7). The ≥95 % concordant analyses have ^{206}Pb/^{238}U ages ranging over *c.* 925–720 Ma. The ≥95 % concordant analyses have ^{206}Pb/^{238}U ages ranging over *c.* 925–720 Ma. From observation of the data in the presented concordia diagram (Fig. 7a), it is apparent that the two youngest analyses have been subjected to Pb loss and have been excluded from further age calculations. The five youngest remaining analyses were conducted on zircon rims, and have therefore been excluded when calculating a crystallization age. A weighted average of these five analyses yields a ^{206}Pb/^{238}U age of 836 ± 10 Ma with MSWD of 0.18 and P-value of 0.95. CL imaging suggests that these rims are likely a later phase of zircon growth, which would have occurred during metamorphism. The remaining 36 concordant analyses gave a ^{206}Pb/^{238}U weighted average age of 887 ± 5 Ma with an MSWD of 1.6 and P-value of 0.020, suggesting a slight over-dispersion of the data. Investigation of the remaining analyses in a weighted average plot (Fig. 7b) resulted in the three oldest grains being excluded from further age calculations. These grains are noticeably older than the remaining population and, as such, may be inherited. The remaining analyses produced an average age of 884 ± 4 Ma with an MSWD of 0.99 and P-value of 0.49 (n = 33), which is interpreted to signify the crystallization of the igneous protolith to this sample.

Thirty-four analyses were conducted on zircons from sample JA15-36 (Fig. 8). Twenty-three of these analyses were shown to be ≥95 % concordant with ages ranging over *c.* 930–790 Ma. Similarly to JA15-26, the youngest six ages were obtained from zircon rims and the abrupt change in age that is again

Figure 3. (Colour online) Structural and lithological maps of the north and south study areas. Jebel Ja'alan is located 50 km south of Sur and 15 km north of Jalan Bani Bu Ali. Grid references refer to WGS84 (Zone 40N) and UTM coordinates. (a) Northern Jebel Ja'alan study area, notably comprising Al Wafi Schist, Ja'alan Gneiss and Ja'alan Granite. The Ja'alan Gneiss can be observed to be thrust over the Al Wafi Schist along the E–W boundary between the lithologies, while the Al Wafi Schist is interpreted to be thrust over the Ja'alan Gneiss along the N–W boundary. Structural data from the northern study area are presented in accompanying stereonets: (i) plunge and plunge-direction of Al Wafi Schist aggregate mineral lineations plotted as points; (ii) dip and dip-direction of Al Wafi Schist axial planes (minor folds) plotted as great circles; (iii) dip and dip-direction of Al Wafi Schist foliations plotted as great circles (grey) and poles (black) (profile plane and pole are shown in red); (iv) dip and dip-direction of Ja'alan Gneiss foliations plotted as great circles (grey) and poles (black) (rofile plane and pole are shown in red); (v) plunge and plunge-direction of Ja'alan Gneiss aggregate mineral lineations plotted as points; and (vi) dip and dip-direction of Ja'alan Gneiss axial planes (minor folds) plotted as great circles. Foliation data from the Al Wafi Schist and Ja'alan Gneiss show opposing groups of NW- and SE-dipping foliations, but with the presence of several close-to-vertical measurements observed within the Al Wafi Schist. Calculating the pole to a profile plane of foliation measurements results in a value of 12→237 for the Al Wafi Schist, and 08→230 for the Ja'alan Gneiss. Measurements of minor fold axial planes within the Ja'alan Gneiss can be seen to be somewhat similar to the spread of foliation data. In comparison, the few measurements in the Al Wafi Schist are more suggestive of approximately N–S-trending folds. Measurements of aggregate mineral lineations in the Al Wafi Schist and Ja'alan Gneiss display a similar trend of gently inclined SSW-plunging lineations. It can be observed that the trend of these lineations are approximately 30° away from the calculated poles to profile planes of the Al Wafi Schist and Ja'alan Gneiss foliation measurements, which may reflect shearing that occurred prior to folding of these lithologies. (b) Southern Jebel Ja'alan study area. The dominant lithology in the study area is the Ja'alan Granite, which is bounded in the SE by hornblendite and by Ja'alan Gneiss in the north. A number of the Brown Dolerite dykes have been interpreted in this study area via satellite photo interpretation.

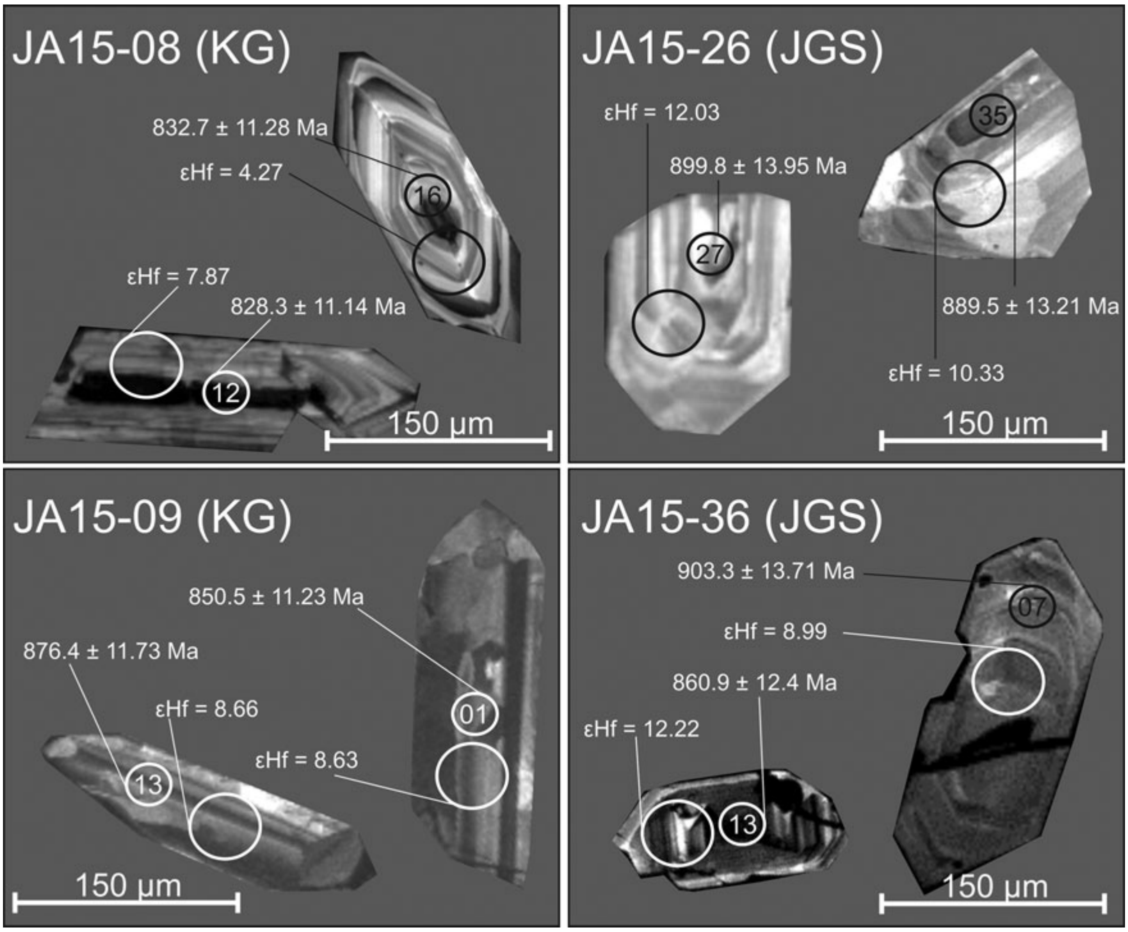

Figure 4. Cathodoluminescence (CL) images of Zircons from samples selected for geochronological analysis. Numbered circles represent LA–ICP–MS spot locations of 30 μm diameter, while accompanying larger circles on each grain represent MC–LA–ICP–MS spot locations. KG – Kamil Granodiorite; JGS – Ja'alan Gneiss.

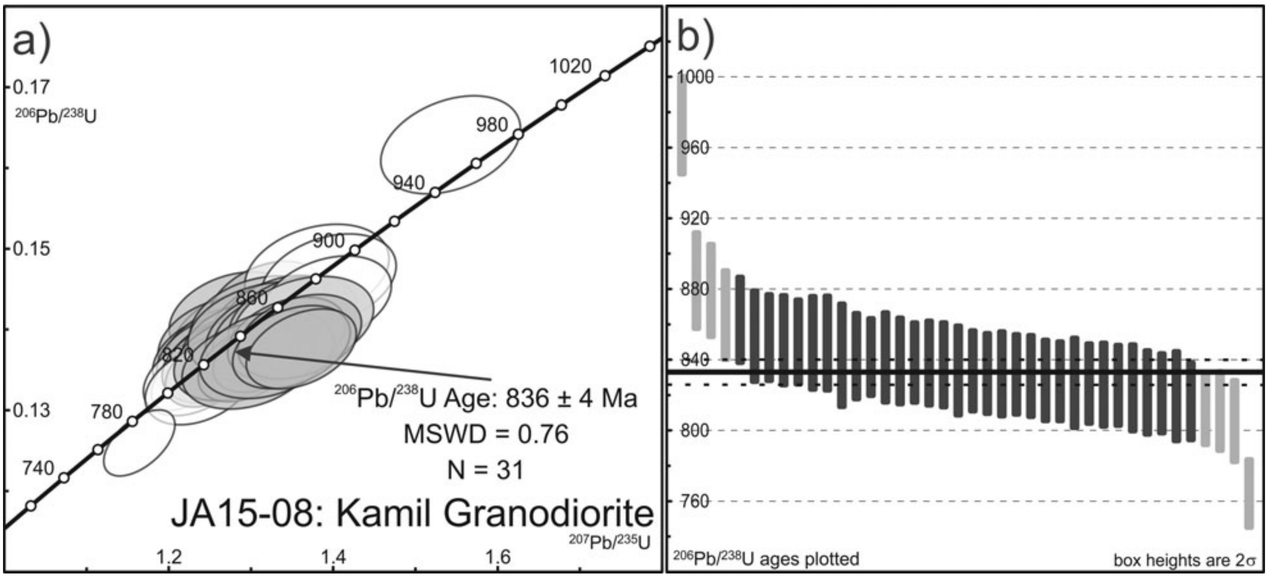

Figure 5. (a) U–Pb concordia diagram for ≥95 % concordant zircons from Kamil Granodiorite sample JA15-08 with 2σ data point error ellipses. Shaded ellipses represent grains used to produce a ^{206}Pb/^{238}U weighted average age, while clear ellipses indicate omitted grains. (b) Age analysis plot of individual ^{206}Pb/^{238}U ages from Kamil Granodiorite sample JA15-08. Analyses are arranged in order of decreasing age from left to right. Dark boxes indicate grains used to produce a ^{206}Pb/^{238}U weighted average age (indicated by the solid black line), while the lighter boxes represent omitted grains.

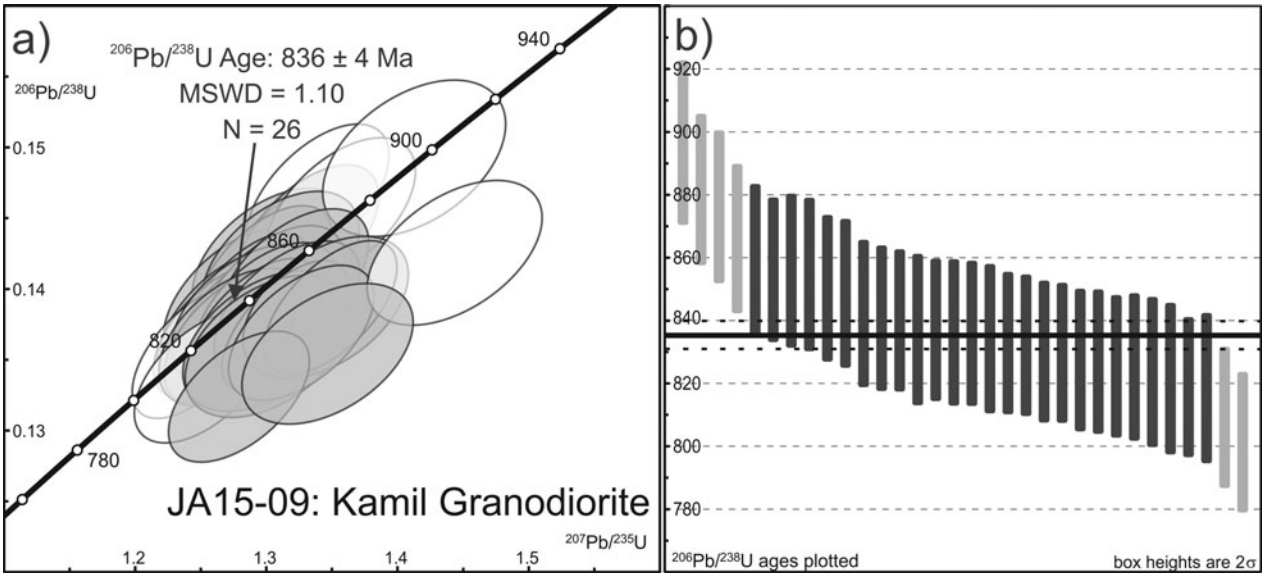

Figure 6. (a) U–Pb concordia diagram for ≥95 % concordant zircons from Kamil Granodiorite sample JA15-09 with 2σ data point error ellipses. Shaded ellipses represent grains used to produce a ^{206}Pb/^{238}U weighted average age, while clear ellipses indicate omitted grains. (b) Age analysis plot of individual ^{206}Pb/^{238}U ages from Kamil Granodiorite sample JA15-09. Analyses are arranged in order of decreasing age from left to right. Dark boxes indicate grains used to produce a ^{206}Pb/^{238}U weighted average age (indicated by the solid black line), while the lighter boxes represent omitted grains.

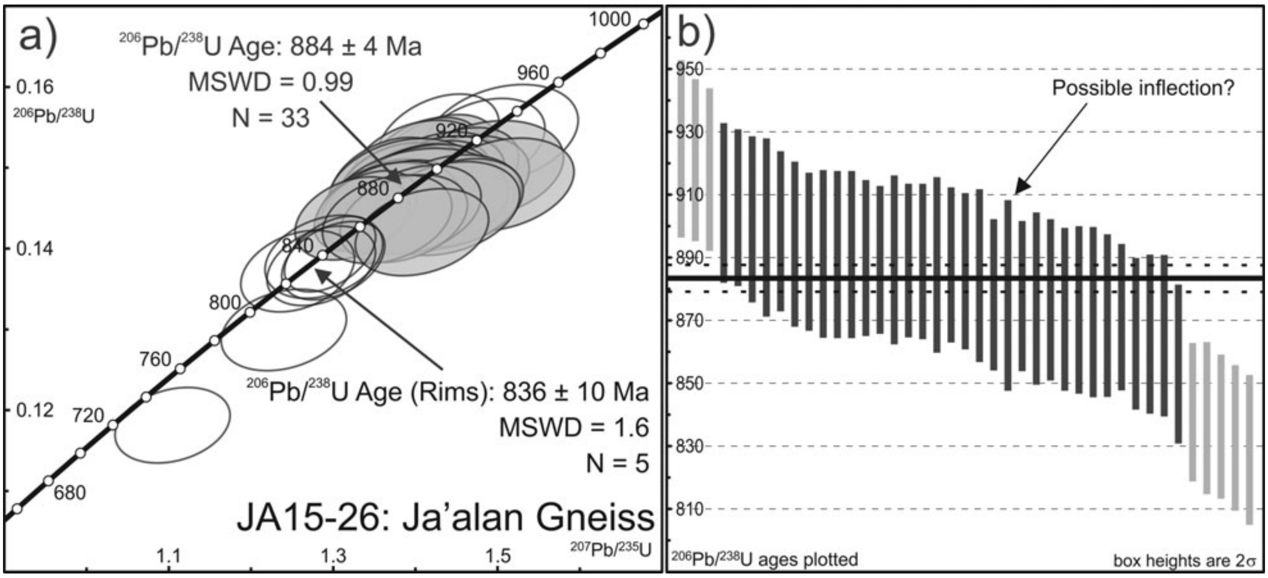

Figure 7. (a) U–Pb concordia diagram for ≥95 % concordant zircons from Ja'alan Gneiss sample JA15-26 with 2σ data point error ellipses. (b) Age analysis plot of individual ^{206}Pb/^{238}U ages from Ja'alan Gneiss sample JA15-26. Dark boxes indicate grains used to produce a ^{206}Pb/^{238}U weighted average age (indicated by the solid black line), which is interpreted to represent the crystallization of the igneous protolith. A possible inflection point is indicated, which may relate to Pb loss. Shading/legend as for Figure 6.

interpreted to be due to a later phase of zircon growth, and have been excluded from the calculation of the crystallization age. These six analyses yield a ^{206}Pb/^{238}U weighted average age of 811 ± 20 Ma with MSWD of 2.4 and P-value of 0.032. A ^{206}Pb/^{238}U weighted average of the remaining 17 analyses yielded an age of 883 ± 11 Ma with an MSWD of 2.8 ($n = 23$). The MSWD suggests that these data do not represent a single age. From further inspection of the data using a weighted average plot (Fig. 8b) it is interpreted that the oldest grain (*c*. 928 Ma) is inherited; it is therefore excluded from further age calculations. A ^{206}Pb/^{238}U weighted average of the remaining analyses ($n = 16$) reveals an age of 880 ± 10 Ma with an MSWD of 2.3 and P-value of 0.17. Such an MSWD still suggests an over-dispersion of the data that may be due to minor unresolved lead loss; this sample has therefore been excluded from any further interpretation.

4.b.3. *Al Wafi Schist monazite*

In situ monazite U–Pb geochronology was undertaken on samples JA15-04, JA15-06, JA15-40 and JA15-43 from the Al Wafi Schist to constrain the age of

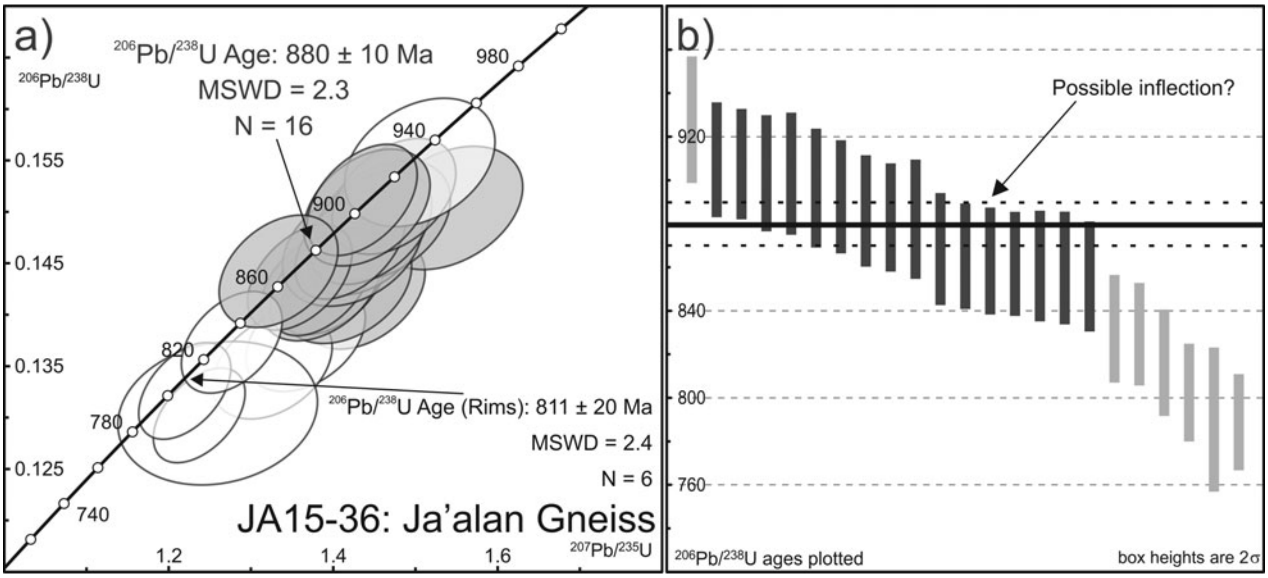

Figure 8. (a) U–Pb concordia diagram for ≥95 % concordant zircons from Ja'alan Gneiss sample JA15-36 with 2σ data point error ellipses. (b) Age analysis plot of individual ^{206}Pb/^{238}U ages from Ja'alan Gneiss sample JA15-36. Shading/legend as for Figures 6 and 7.

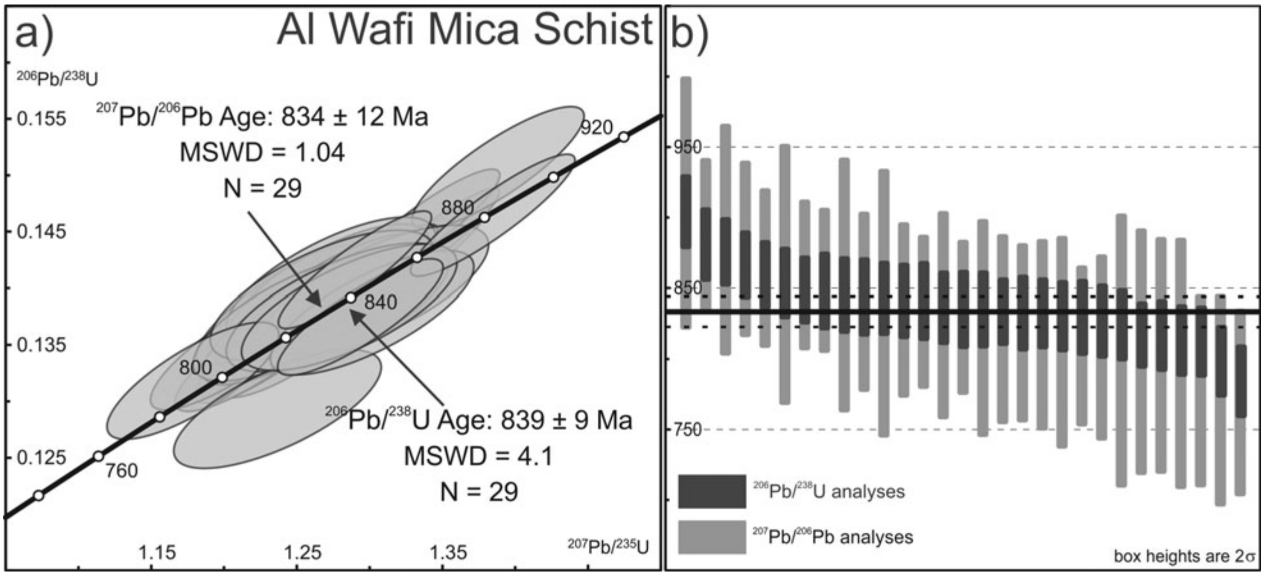

Figure 9. (a) U–Pb concordia diagram for ≥95 % concordant monazite grains from Al Wafi Schist samples JA15-04, JA15-06, JA15-40, JA15-43 with 2σ data point error ellipses. Shaded ellipses represent grains used to produce ^{206}Pb/^{238}U and ^{207}Pb/^{206}Pb weighted average ages. (b) Weighted average plot of individual ^{206}Pb/^{238}U (dark grey) and ^{207}Pb/^{206}Pb (light grey) ages from Al Wafi Schist samples. All analyses have been used to produce a ^{207}Pb/^{206}Pb weighted average age, which is indicated by the solid black line.

metamorphism. Individual analyses are provided in the supplementary material. Monazite is abundant within the matrix of these samples, although commonly at sizes unsuitable for U–Pb isotopic analysis ($<10\ \mu$m). However, a total of 29 analyses were obtained from unzoned grains located within the matrix. Data are displayed on Wetherill concordia plots and weighted mean plots of ^{206}Pb/^{238}U age (Fig. 9). All U–Pb analyses of monazite from the Al Wafi Schist are >95 % concordant and reveal a large spectrum of ^{206}Pb/^{238}U ages (*c.* 905–780 Ma). A ^{206}Pb/^{238}U weighted average of all analyses yields an age of 839 ± 9 Ma with an MSWD of 4.1 (n = 29). Inspection of the plotted U–Pb ages revealed a spread of ages, indicating that the older and younger analyses are slightly discordant. Using the ^{207}Pb/^{206}Pb ages obtained from the analysed grains yields a weighted average age of 834 ± 12 Ma, with an MSWD of 1.04 and P-value of 0.41 (n = 29), which is within error of the zircon rim ages obtained from the Ja'alan Gneiss samples. The ability to calculate a coherent age from the obtained ^{207}Pb/^{206}Pb ages, and not the obtained ^{206}Pb/^{238}U ages, indicates there is a U/Pb calibration uncertainty not included in the presented analytical errors. Because of this, the obtained ^{207}Pb/^{206}Pb weighted average age is interpreted to best signify the time at which the

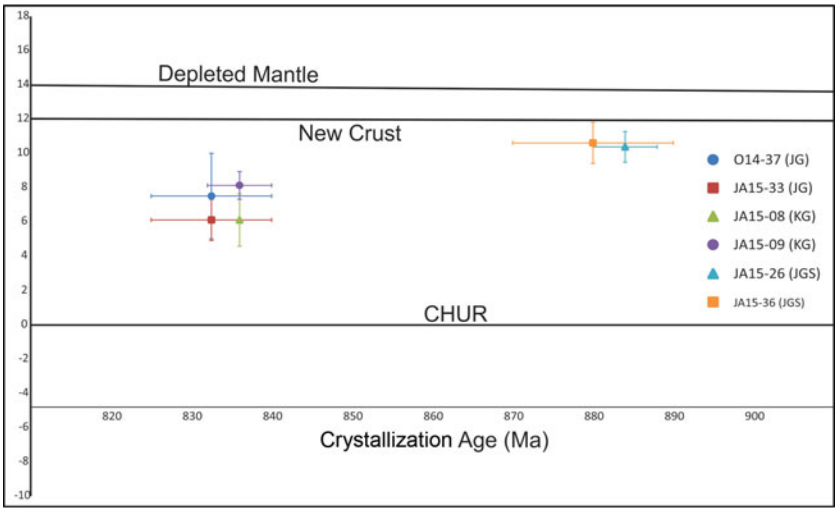

Figure 10. (Colour online) εHf versus ^{206}Pb/^{238}U age plot for igneous lithologies from Jebel Ja'alan. The depleted mantle line of Griffin *et al.* (2002) is plotted, as is the new crust line obtained by Dhuime, Hawkesworth & Cawood (2011). Weighted εHf values are given at the interpreted U–Pb crystallization age for each lithology. Errors for age and εHf values are shown at the 2σ level. The *c.* 840–820 Ma age range obtained by Whitehouse, Pease & Al Khirbash (2016) is used for the Ja'alan Granite. The plot shows a general trend that suggests all samples are becoming more evolved with time. JG – Ja'alan Granite; KG – Kamil Granodiorite; JGS – Ja'alan Gneiss.

Al Wafi Schist experienced near-peak metamorphic conditions.

4.c. Zircon Lu–Hf isotopes

The Lu–Hf isotope system enables assessment of the chemical differentiation of the silicate Earth (crust and mantle), as fractionation of Lu from Hf effectively occurs during mantle melting (Hawkesworth & Kemp, 2006). Zircon effectively preserves the initial ^{176}Hf/^{177}Hf ratio of the magma from which it formed, providing a persistent record of the Hf isotopic composition of the source environment at the time of crystallization (Payne *et al.* 2016). Hafnium isotope analyses were obtained for select igneous and metaigneous lithologies found in Jebel Ja'alan, specifically the Ja'alan Granite, Kamil Granodiorite and Ja'alan Gneiss. Data are plotted on εHf v. time plots (Fig. 10); individual analyses are available in the supplementary material.

4.c.1. Ja'alan Granite

Nineteen zircons from the Ja'alan Granite (O14-37 and JA15-33) were analysed for hafnium isotopes. Seventeen of the spots returned εHf values ranging between +2.30 and +10.17, suggesting relatively juvenile sources with relatively low crustal involvement.

4.c.2. Kamil Granodiorite

Twenty-nine zircons from the Kamil Granodiorite (JA15-08 and JA15-09) were also analysed for hafnium isotopes. The εHf values obtained from this lithology range from +4.3 to +10, again suggesting a juvenile source. A single analysis value of –0.8 was obtained for this lithology.

4.c.3. Ja'alan Gneiss

Thirty-one zircons from the Ja'alan Gneiss (JA15-26 and JA15-36) were used for hafnium analysis. The zircons displayed εHf values between +7.6 and +13.3, which indicates these grains were formed in a juvenile melt with minor involvement of older crust.

4.d. ^{40}Ar/^{39}Ar geochronology

^{40}Ar/^{39}Ar data were obtained from muscovite grains separated from the Ja'alan Granite and Al Wafi Schist (Fig. 11). The Ja'alan Granite sample, JA15-03, yielded a weighted average plateau age of 831 ± 15 Ma with a MSWD of 0.30, P-value of 0.89 and 100 % of ^{39}Ar released. The Al Wafi Schist sample (JA15-04) displays two plateau ages of 831 ± 7 Ma and 827 ± 15 Ma, with a combined weighted average plateau age of 830 ± 6 Ma (MSWD 0.22; P-value 0.99). These data suggest that the granite and country rocks had cooled below the muscovite closure temperature of *c.* 350–405 °C (Hodges, 1991; Hames & Bowring, 1994; Harrison *et al.* 2009) by this time.

4.e. Sm–Nd radiogenic isotopes

Five samples were selected for Sm–Nd isotope analysis. These five samples represent the dominant igneous lithologies encountered in southern Jebel Ja'alan: Ja'alan Granite; 'Grey Dolerite'; andesite; 'Brown Dolerite'; and hornblendite. All five samples yielded positive εNd values between +0.56 and +6.78, plotting between the depleted mantle (DM) and chondrite universal reservoir (CHUR) values demonstrating the juvenile nature (Fig. 12). The isotopic evolution of JA15-18 (Ja'alan Granite) is plotted on Figure 12, showing the depleted mantle model age of *c.* 1291 Ma

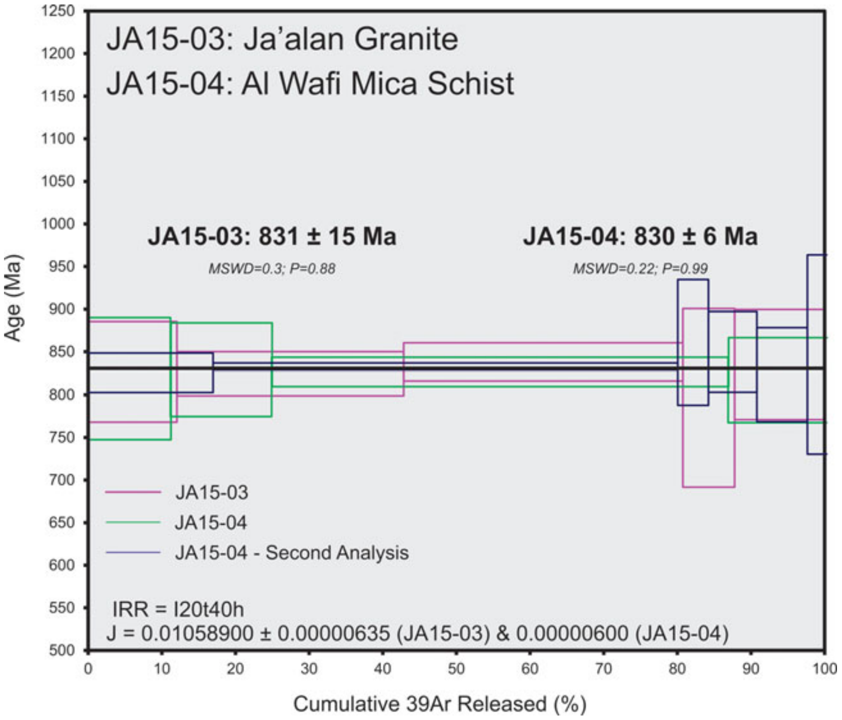

Figure 11. (Colour online) ^{40}Ar/^{39}Ar muscovite age data plot for Ja'alan Granite sample JA15-03 and Al Wafi Schist sample JA15-04. The Ja'alan Granite (pink) sample displays a weighted average plateau age of 831 ± 15 Ma (MSWD 0.30). The Al Wafi Schist (green and blue) sample displays a weighted plateau age of 830 ± 6 Ma (MSWD 0.22).

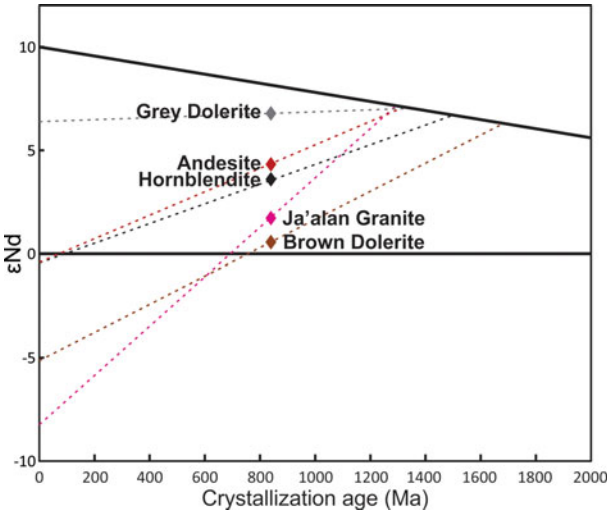

Figure 12. (Colour online) εNd versus time plot showing samples JA15-14 (Grey dolerite), JA15-18 (Ja'alan Granite), JA15-25 (hornblendite), JA15-34 (andesite), JA15-42 (Brown dolerite). Evolution lines for each sample are represented by the dashed lines. The depleted mantle line shown is that obtained by Goldstein, O'nions & Hamilton (1984).

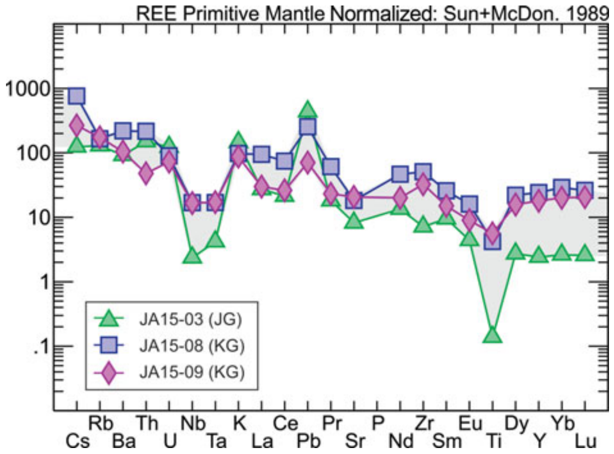

Figure 13. (Colour online) Rare Earth element (REE) spider plot for samples from the Ja'alan Granite (JA15-03) Kamil Granodiorite (JA15-08 and JA15-09) normalized to primitive mantle (Sun & McDonough, 1989). All samples display a general decrease in elemental abundance with increasing atomic weight, in addition to distinct negative Nb, Ta and Ti anomalies as well a positive Pb anomaly.

and a εNd ($t = 0$) value of –8.23. The DM model ages for samples from the other lithologies are all Mesoproterozoic in age and older than the Ja'alan Granite model age, despite field relationships clearly indicating that they were emplaced after the granite. Most notably, the latest intrusion (JA15-42) has the oldest model age (*c.* 1663 Ma), suggesting an increase in crustal contamination in parent magma with time.

4.f. Trace-element geochemistry

Trace elements were analysed for two samples of Kamil Granodiorite (JA15-08 and JA15-09) and a single sample of Ja'alan Granite (JA15-03). Figure 13 is a rare Earth element (REE) spider plot that shows how enriched or depleted in REEs each sample is when compared to primitive mantle (Sun & McDonough, 1989). The REE spider plot demonstrates that the Ja'alan Granite and Kamil Granodiorite are enriched

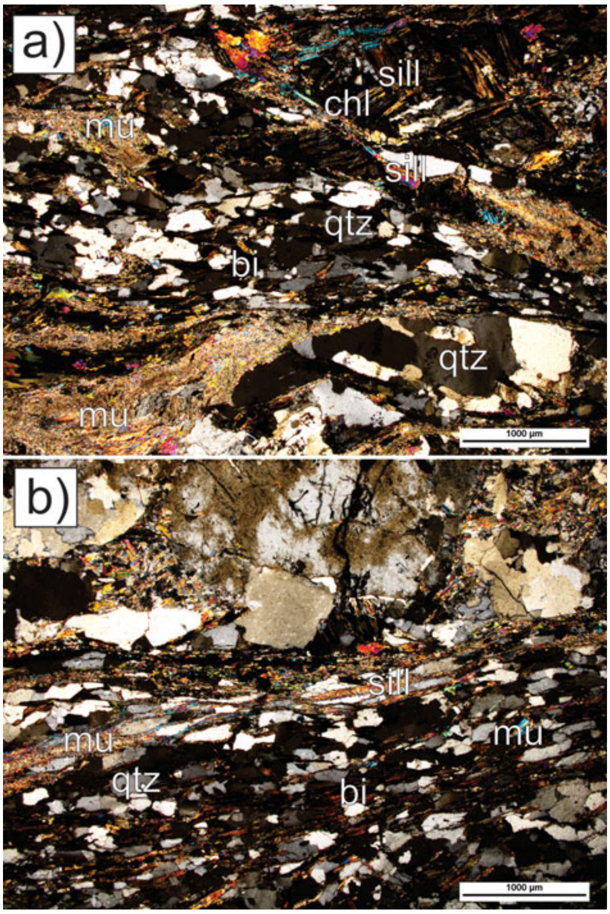

Figure 14. (Colour online) Photomicrographs of petrological relationships within Al Wafi Schist sample JA15-43, which has been used for phase equilibria modelling. (a) A strong fabric of relatively fine-grained muscovite that can be seen to cross-cut quartz grains. A smaller fabric of biotite can also be seen to run parallel to this fabric of muscovite; the biotite grains in this fabric are often separated by quartz grains. Sillimanite is also observed in the sample and can be seen to be loosely aligned with the biotite and muscovite fabrics; it can also be seen to be in contact with chlorite. Deformed sillimanite rosettes can also be observed. (b) A strong fabric defined by biotite, muscovite and sillimanite that wraps around quartz grains. Muscovite within the fabric is very fine relative to other minerals in the sample. There are also larger muscovite grains that are separated by quartz. Biotite grains can also be observed to be separated from each other by quartz grains, and also contain inclusions of quartz in some instances.

in the light REEs with a general decrease in elemental abundance with increasing atomic weight. All three samples show distinct negative Nb, Ta and Ti anomalies relative to primitive mantle, in addition to positive Pb anomalies relative to primitive mantle.

4.g. Petrography

Samples from the metapelitic Al Wafi Schist (JA15-04, JA15-43) were used for phase equilibria modelling; as such, a detailed petrographic analysis was undertaken for this lithology. Results of the petrographic analysis of JA15-04 can be found in the supplementary material. JA15-43 (Fig. 14) contains quartz, plagioclase, biotite, muscovite, garnet and sillimanite with minor ilmenite, magnetite and chlorite. In this sample fine-grained (0.2–0.3 mm) garnet is present with euhedral grain shape, albeit partially elongate, and contains inclusions of quartz. The matrix comprises fine (0.1–0.3 mm) anhedral quartz and subhedral plagioclase, with quartz forming the majority of the matrix. This sample has a coarse-grained (1–2 mm) matrix of quartz and plagioclase in addition to the finer-grained matrix observed for the other Al Wafi Schist samples. A fabric of relatively fine-grained muscovite can be seen to cross-cut quartz and a smaller number of plagioclase grains. In this sample a smaller fabric of biotite can also be seen to run parallel to this fabric. The biotite grains in this fabric are often separated by quartz and plagioclase grains. Sillimanite is also observed in the sample and can be seen to be loosely aligned with the biotite and muscovite fabrics; it can also be seen to be in contact with chlorite. Deformed sillimanite rosettes can also be observed throughout this sample. On the basis of grain characteristics and distribution, as well as textural relationships between minerals, the interpreted peak assemblage for this sample is quartz–plagioclase–muscovite–sillimanite–biotite–ilmenite–magnetite–garnet. Post-peak metamorphism in each sample is restricted; the separation of biotite and muscovite by fine-grained (0.1–0.3 mm) chlorite is observed within each sample, interpreted as retrograde alteration.

4.h. Mineral chemistry

Full microprobe analyses for silicate minerals in Al Wafi Schist samples JA15-04, JA15-41 and JA15-43 are given in the supplementary material. Compositional transects were obtained for two garnet grains in Al Wafi Schist samples JA15-41 and JA15-43. Both transects show similar patterns of decreasing Mg from core to rim of each grain, and increasing Mn from core to rim.

4.i. *P–T* pseudosections

Two samples of the Al Wafi Schist (JA15-04 and JA15-43) were used for phase diagram calculations. T–M_O and T–M_{H2O} diagrams were calculated to constrain the amount of FeO v. Fe_2O_3 and H_2O present in each sample prior to pressure–temperature (*P–T*) modelling. The associated *T–M* pseudosections, as well as the *P–T* pseudosection for sample JA15-04, are presented in the supplementary material.

The *P–T* pseudosection calculated for Al Wafi Schist sample JA15-43 is presented in Figure 15. The staurolite stability field is 'V'-shaped and is stable above *c.* 2.5 kbar, with the stable temperature range increasing with pressure. Garnet is stable throughout much of the diagram for this sample, with stability generally increasing with decreasing temperature. The interpreted peak mineral assemblage quartz–

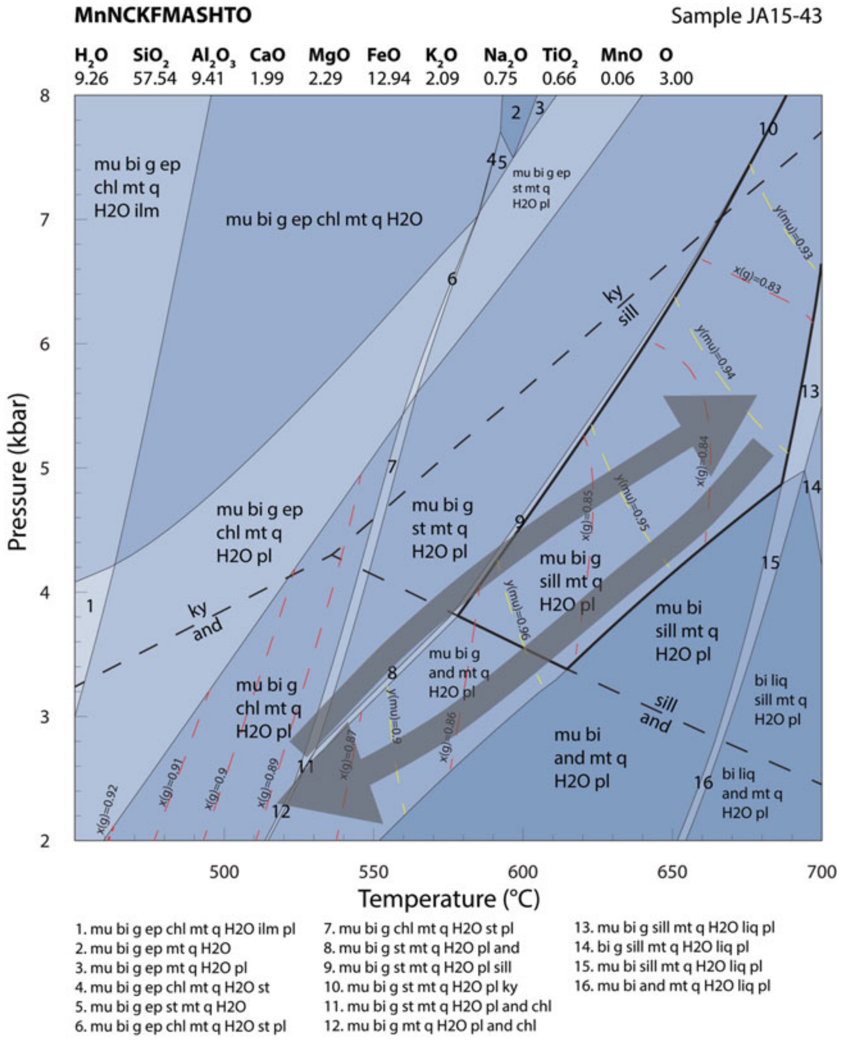

Figure 15. (Colour online) Calculated *P–T* pseudosection for sample JA15-43 from the Al Wafi Schist. The bulk composition used for modelling is given in the top of the diagram and expressed as mole percent. The field muscovite–biotite–ilmenite–plagioclase–magnetite–sillimanite–garnet–quartz–H_2O (shown with bold outline) corresponds to the peak assemblage and occurs within the *P–T* range of *c.* 3.2–7.6 kbar at 580–700 °C. Interpreted prograde and retrograde *P–T* paths are shown by the grey arrows. Dashed lines represent compositional variable contours of muscovite (yellow – $y(\mathrm{mu}) = \mathrm{Al}^{VI}$ cations) and garnet (red – $x(\mathrm{g}) = \mathrm{Fe}^{2+}/(\mathrm{Fe}^{2+} + \mathrm{Mg})$ cations).

plagioclase–muscovite–sillimanite–biotite–ilmenite–magnetite–garnet for JA15-43 is stable within the *P–T* range of *c.* 3.2–7.6 kbar at 580–700 °C.

5. Discussion

5.a. Structural history

Two inconsistencies can be found in the structural data collected from the northern study area. First, foliation measurements of the Al Wafi Schist are dominantly NE-dipping, while the opposite holds true for the Ja'alan Gneiss. This is interpreted to represent measurements of these lithologies being taken on opposing limbs of E–W-trending folds in the area, suggesting that near-horizontal planes have been measured in close proximity to a fold hinge. The second discrepancy is the *c.* 35° variation between aggregate mineral lineations and calculated fold hinges. We interpret that this may be the result of shearing that has occurred prior to the folding of both units. Restoring these measurements to pre-folding values gives an approximate trend of 55→115 for plunge and plunge direction.

The structures observed in the study area are indicative of multiple regional-scale deformation events affecting the region, interpreted to occur both during and post metamorphism. Aggregate mineral lineations observed in the Al Wafi Schist and Ja'alan Gneiss are interpreted to have originally formed as a result of shearing that occurred prior to these main deformation events. The first deformation event (D_1) involved the top-to-the-NNE thrusting of the Ja'alan Gneiss over the Al Wafi Schist, the creation of approximately E–W-trending folds (F_1; Fig. 3), and the generation of the foliation planes (S_1) observed within the study area (Fig. 3). Both field and petrographic observations are suggestive of this deformation occurring at high temperatures; this event is therefore interpreted to be contemporaneous with or slightly postdating peak metamorphism (*c.* 835 Ma). The second deformation event (D_2) resulted in a series of structures interpreted to have formed within an E–W compressional stress regime. It is during this period of deformation that top-to-the-east thrusting of the Al Wafi Schist over the Ja'alan Gneiss is interpreted to have occurred. This is in addition to the creation of the two broad, approximately N–S-trending folds (F_2) and a heterogeneously developed crenulation cleavage (S_2) observed to the north of the study area. The timing of this second deformational period is difficult to constrain; however, Filbrandt, Nolan & Ries (1990) observe E–W compressional structures within the overlying Simsima Formation, which would constrain the age of deformation to being younger than Maastrichtian.

5.b. Age and tectonic environment of formation of Jebel Ja'alan basement

5.b.1. Early intrusives

U–Pb zircon data were recently obtained for the Ja'alan Granite Batholith by Whitehouse, Pease & Al Khirbash (2016); these authors constrained crystallization of the batholith to 840–825 Ma. Zircons from the Ja'alan Granite gave positive εHf values between +2.30 and +10.17, indicating that the batholith originates from a juvenile mantle source with only limited crustal input. The single sample (JA15-18) analysed for Sm–Nd also returned a positive εNd value of +1.72. The whole-rock Nd data yield more evolved values than the single zircon grain Hf values, which is indicated by the different model ages. The Hf depleted mantle model ages ranged between 990 Ma and 1220 Ma with an average of 1130 Ma, whereas the Nd model age yielded an older age of 1291 Ma. We suggest that this is due to assimilation of country rock in an evolving magma. Zircon, forming early in the cooling history, is preserving more juvenile isotopic values (i.e. younger 'model' ages) than the bulk rock that has been affected by post-zircon crystallization assimilation/mixing of more country rock. This later contamination is reflected in the older whole-rock Nd model age and may explain the apparent discrepancy between the two isotopic/sample systems.

U–Pb data from Kamil Granodiorite samples JA15-08 and JA15-09 both yielded rounded ages of 836 ± 4 Ma. This age is interpreted as the age of crystallization for the Kamil Granodiorite, which falls within the suggested timing of metamorphism for the Al Wafi Schist and Ja'alan Gneiss as well as the age of emplacement and crystallization of the Ja'alan Granite. Due to its coarse texture and relative lack of deformation (Fig. 2), we interpret that the Kamil Granodiorite intruded towards the end of the tectonometamorphic event. εHf values obtained for grains from the Kamil Granodiorite (+4.3 to +10) suggest a juvenile origin with limited crustal input for this lithology.

Ja'alan Gneiss sample JA15-26 yielded zircon $^{206}Pb/^{238}U$ average ages of 884 ± 4 Ma, which is interpreted to represent the crystallization age of the igneous, likely granitic, protolith to the Ja'alan Gneiss. This crystallization age is younger, but in broad agreement with that obtained by Whitehouse, Pease & Al Khirbash (2016; 900–880 Ma). The younger age obtained in this study may be a result of Pb loss during a rim growth event. A possible inflection is observable in the weighted average plot presented for sample JA15-26 (Fig. 7b), which could reflect Pb loss. A similar feature is observable for sample JA15-36 (Fig. 8b). Excluding the analyses to the left of this inflection in sample JA15-26 yields a weighted average age of 892 ± 6 Ma, with MSWD of 0.34 and P-value of 0.997. Zircons from the Ja'alan Gneiss gave positive εHf values, ranging from +7.6 to +13.3. These values suggest that the Ja'alan Gneiss protolith formed in a juvenile melt, with any recycling of older crust being minor.

The REE multi-element plot shows that the Ja'alan Granite and Kamil Granodiorite display an overall decrease in normalized enrichment compared to the primitive mantle line with increasing atomic number. Furthermore, the samples display clear negative Nb and Ta anomalies relative to primitive mantle, in addition to positive Pb anomalies. These negative anomalies are characteristic of volcanic-arc magmas due to the low solubility of Nb and Ta in water-rich, solute-poor fluids in the shallow parts of a subduction zone (Baier, Audétat & Keppler, 2008). The positive Pb anomalies also suggest a volcanic-arc origin for the analysed samples, as volcanic-arc magma sources are enriched in mantle-derived lead (Miller, Goldstein & Langmuir, 1994). We therefore interpret that the basement of Jebel Ja'alan formed in a juvenile arc environment.

5.b.2. Dyke swarm

Three separate lithologies comprise the dyke swarm observed in Jebel Ja'alan: the early 'Grey Dolerite'; andesite; and the late 'Brown Dolerite'. Each dyke lithology is temporally distinct as is demonstrated by the clear cross-cutting relationships observed in outcrops. The εNd values of the dykes were all positive and plotted between the depleted mantle and CHUR line (Fig. 12). This suggests that the dyke swarm has a juvenile mantle origin, similar to the juvenile mantle origin of the Ja'alan Granite. With decreasing relative age the separate dyke generations decrease in juvenility, where the 'Grey Dolerite' is the most juvenile (εNd = +6.78), followed by the andesite (+4.32) and then the 'Brown Dolerite' as the most isotopically evolved (+0.56). The depleted mantle model ages for all generations were derived from Sm–Nd data and are older than the DM model age of the Ja'alan Granite. From field observations these model ages do not simply fit the cross-cutting relationships, as it is expected that the model ages would decrease in age from the Ja'alan Granite to 'Brown Dolerite' if the magma reflected consistent mantle input over time. This apparent discrepancy could be due to the higher ^{147}Sm/^{144}Nd ratios recorded by the dykes, which result in the dykes having shallow angle intercepts with the DM line (Fig. 12). These shallow intercepts, in conjunction with uncertainties in the model curve, may be the reason why the granite has the youngest model age. If however real, the isotopic change could be due to increased continental material contaminating the mantle wedge over time from the lower plate. Elburg & Foden (1998) provided evidence from Sulawesi, Indonesia that ^{143}Nd/^{144}Nd variations can show a changing magma evolution due to variation in the magma source (i.e. mantle wedge and subducting slab). This suite of Nd data indicates that the model ages may have been distorted by the progressive assimilation of older sediment off the subducting slab into the mantle wedge, significantly contaminating the lithospheric mantle beneath the Ja'alan arc terrane. The decreasing juvenility in the dyke generations supports this idea of progressive sediment/crustal contamination in the mantle wedge that was tapped by the suite of dykes. An alternative reason for these model ages is that the dykes melted and progressively assimilated more basement schist and gneiss with time (e.g. Pandey *et al.* 1997); we suggest that this is a less likely scenario, however.

5.c. *P–T–t* path of metamorphism

Mineralogical and textural features, as well as compositional variations in muscovite and garnet provide constraints on the metamorphic history of basement rocks in Jebel Ja'alan. The pseudosection (Fig. 15) was contoured for the composition of garnet (x(g) = Fe/(Fe + Mg) cations) and muscovite (y(mu) = Al^{VI} cations). In sample JA15-43, the measured composition of muscovite grains is inconsistent with that calculated for the interpreted peak assemblage field (being greater than any value calculated for that field), but suggest peak conditions are located in the higher-temperature portion of the peak field, likely 650–700 °C at 4–7.5 kbar. The discrepancy between the measured and calculated compositions of muscovite grains within this sample may be a result of ferric iron present in analysed grains that cannot be accounted for by cation calculation procedures. Ferric iron will cause EPMA measured y(mu) values to increase (e.g. Diener & Powell, 2010). Measured compositions of garnet in sample JA15-43 show decreasing Mg from the core to rim of grains, and increasing Mn from core to rim. These patterns have been previously suggested by Tuccillo, Essene & Van Der Pluijm (1990) to represent a diffusional retrograde effect, where resorption of garnet to form biotite enriches garnet in Fe relative to Mg. Additionally, as Mn does not easily incorporate into biotite, this forms an enrichment of Mn on the garnet rim. These variations in mineral chemistry are reflected in the measured x(g) (= Fe^{2+}/(Fe^{2+} + Mg) cations) values, and are able to be correlated with the calculated x(g) values for sample JA15-43 to constrain the retrograde *P–T* conditions and path trajectory. The trajectory of the retrograde path is further constrained by the absence of retrograde staurolite and epidote in the sample, suggesting that retrograde *P–T* conditions were not amenable to the growth of these minerals. The EPMA measured x(g) values, when compared to the calculated values, suggest that the sample decreased to 510–540 °C and 2–2.6 kbar after peak metamorphism, which is corroborated by the presence of chlorite in the retrograde assemblage. A prograde path is difficult to interpret for this sample but, based on similarities to samples JA15-04 and JA15-06, a trajectory passing through the staurolite stability field may be possible due to the presence of this mineral in the peak assemblages of these samples.

U–Pb age data from matrix monazite grains from three Al Wafi Schist samples preserve a ^{207}Pb/^{206}Pb weighted mean age of 834 ± 12 Ma with an MSWD of 1.04. This age is interpreted to reflect near-peak metamorphism, as monazite has been shown to grow in metapelites from *c.* 525 °C (e.g. Wing, Ferry & Harrison, 2003; Corrie & Kohn, 2008), remaining closed to lead loss at or above sillimanite stability (Smith & Barreiro, 1990). ^{40}Ar/^{39}Ar age data from muscovite grains located within the Al Wafi Schist yield a plateau age of 830 ± 6 Ma. Hodges (1991) and Hames & Bowring (1994) argue that plateau ages from high-temperature rocks represent a closure temperature of *c.* 350 °C in muscovite grains; more recently however, the closure temperature has been suggested by Harrison *et al.* (2009) to be within a range of *c.* 350–405 °C, still considerably cooler than peak temperatures experienced by the schist (*c.* 650–700 °C). It is interpreted that since the muscovite ^{40}Ar/^{39}Ar age is within error of the calculated ^{206}Pb/^{238}U weighted average monazite age cooling and exhumation likely occurred relatively rapidly, cooling by *c.* 300 ± 50 °C within 0–22 Ma. Muscovite grains obtained from the Ja'alan Granite yielded a similar age of 831 ± 15 Ma, suggesting that the timing of cooling obtained for the Al Wafi Schist was coeval with cooling of the Ja'alan Granite.

The interpreted *P–T* path, constrained via linking the measured compositions of minerals to calculated phase compositions as well as via petrographic observations related to mineral stability fields, suggests a clockwise *P–T* path for rocks in Jebel Ja'alan. The *P–T* conditions correspond to a Barrovian apparent thermal gradient (e.g. Stüwe, 2007; Kelsey & Hand, 2015), approximately 93.3–162.5 °C/kbar. Such a range in apparent thermal gradient can be consistent with what is associated with an active arc setting as shown in a variety of locations (e.g. Bard, 1983; Zhao *et al.* 2001; Brown, 2007; Abu El-Enen, 2011; Jarrar *et al.* 2013). If the thermal gradient is indeed associated with an active arc setting, this would be consistent with the tectonic setting interpreted from the trace-element data for the Ja'alan Granite and Kamil Granodiorite.

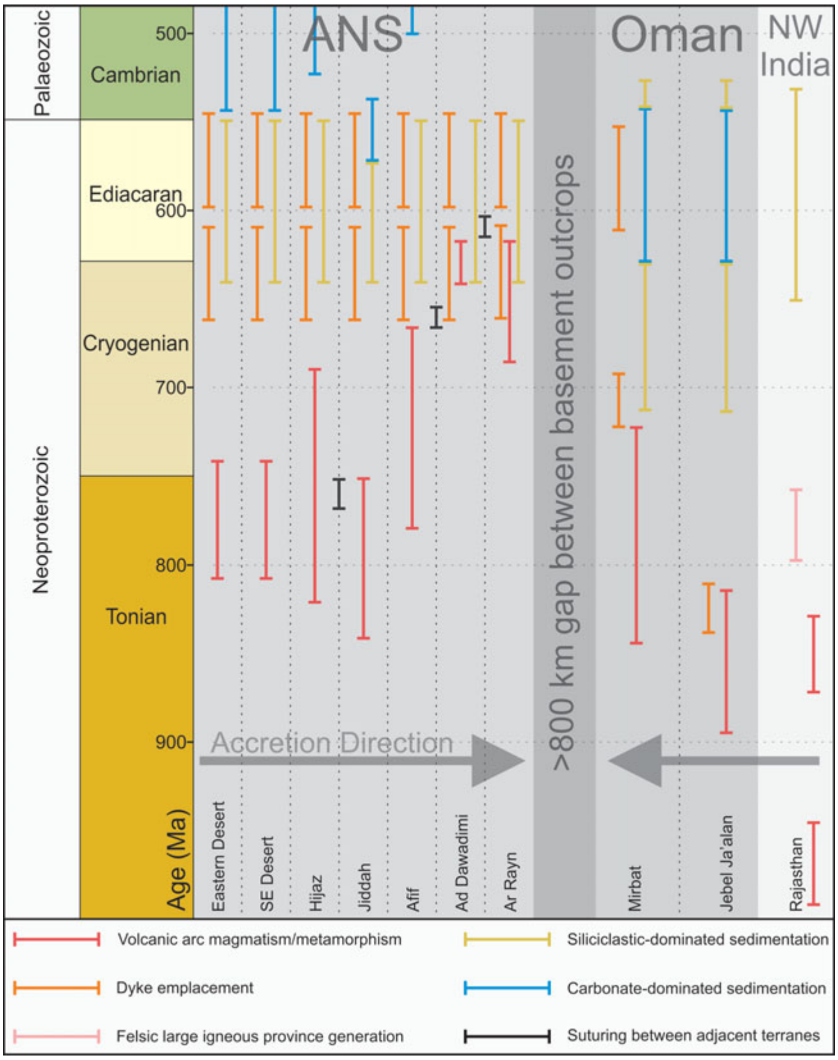

Figure 16. (Colour online) Time–space plot for terranes in the Arabian–Nubian Shield, Oman and NW India. The gap between the ANS and Oman signifies a >800 km gap between the closest basement outcrops. It can be observed that the timing of arc magmatism and metamorphism as well as suturing of terranes decreases to the modern day east of the ANS, reflecting progressive amalgamation of younger arc terranes. The opposite trend can be seen within NW India and the Omani basement, with ages decreasing towards the modern-day west. It can also be seen that accretion in Oman finished earlier than in the ANS, reflected in the earlier deposition of sediments. Ages displayed for the ANS are from Allen (2007) and Johnson *et al.* (2011); ages displayed for Oman are from Allen (2007), Rantakokko *et al.* (2014) and this study. Ages displayed for Rajasthan are compiled from the following studies: Haldar & Deb (2001); Buick *et al.* (2006); Gregory *et al.* (2009); Van Lente *et al.* (2009); Just *et al.* (2011); Cozzi, Rea & Craig (2012); Raza *et al.* (2012); Ashwal *et al.* (2013); Davis, Meert & Pandit (2014).

5.d. Regional implications

In this study we document the Tonian juvenile volcanic-arc nature of the magmatic rocks of the Jebel Ja’alan basement of NE Oman. This confirms the interpretations of earlier studies in the region (Gass *et al.* 1990) and also of studies from other Omani basement regions (Allen, 2007; Bowring *et al.* 2007; Rantakokko *et al.* 2014). We interpret the igneous suite of Jebel Ja’alan to relate to the Tonian subduction of the Mozambique Ocean that separated Neoproterozoic India from the Neoproterozoic African continents. This tectonic setting is broadly similar to the inferred tectonic setting of many of the terranes of the ANS, which are thought to be predominantly intra-oceanic island arcs formed within the same Mozambique Ocean (Johnson & Woldehaimanot, 2003; Meert, 2003; Collins & Pisarevsky, 2005; Johnson *et al.* 2011; Cox *et al.* 2012; Robinson *et al.* 2014; Blades *et al.* 2015; Robinson, Foden & Collins, 2015*a*, *b*). *P–T* paths interpreted in this study are also similar to those interpreted for ANS terranes. For example, the Al Wafi Schist shares very similar peak *P–T* conditions and retrograde path trajectory to those reported by Abu-Alam *et al.* (2014) from the Baladiyah Complex, Saudi Arabia. When compared to terranes in Egypt, it can be seen that Al Wafi Schist experienced higher temperatures and lower pressures than rocks of the Central Eastern Desert terrane (Fritz *et al.* 2002), which contrasts with results from the Sinai Peninsula (Abu El-Enen, 2011) where lower peak *P–T* conditions are recorded. Despite variations in peak *P–T* conditions, retrograde

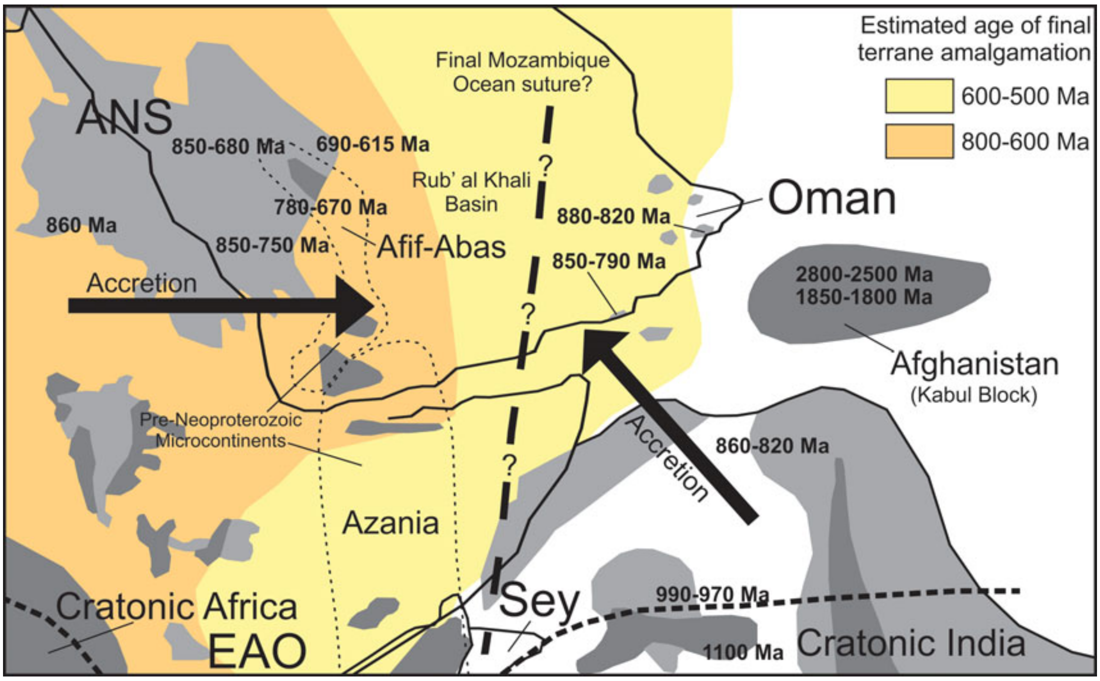

Figure 17. (Colour online) Geological outcrop map of the ANS, Oman and India in Gondwana adapted from Collins and Pisarevsky (2005). Outcrops older than 1000 Ma are shown in dark grey, while those younger are shown in light grey. Protolith ages displayed mark arc-terrane formation and accretion within the ANS, Oman and NW India. Interpreted directions of accretion are shown for the ANS and India/Oman by the black arrows. The black dashed line marks the possible final suture of the Mozambique Ocean, and is almost coincident with the boundary between structural domains two and three in figure 3 of Stern and Johnson (2010). Basement ages recently obtained by Faryad *et al.* (2016) for the Kabul Block in Afghanistan are also displayed. These ages correlate with detrital zircon age ranges obtained by Whitehouse, Pease & Al Khirbash (2016) for the Al Wafi Schist and may represent a possible sediment source. EAO – East African Orogen; Sey – Seychelles.

trajectories are broadly similar across these terranes; likewise, there is no large discrepancy between the thermal gradients experienced between these terranes, which suggests that similar tectonic settings are responsible for metamorphism in these regions.

Where the Omani basement and the ANS differ is in the timing and polarity of arc accretion (Figs 16, 17). Arc magmatism and accretion in Jebel Ja'alan is similar to some of the oldest arc magmatism in west Saudi Arabia (*c.* 850 Ma; Robinson *et al.* 2014). As one moves east in Saudi Arabia the arc magmatism and accretion-related deformation/metamorphism becomes younger until, in the Ar Rayn Terrane (the easternmost exposed terrane; Fig. 1), subduction-related magmatism is still active at *c.* 600 Ma (Doebrich *et al.* 2007) with coeval terrane deformation and metamorphism (Johnson *et al.* 2011; Cox *et al.* 2012). To the south of the Saudi ANS in Yemen, the Al-Mukalla terrane (Fig. 1) is interpreted as a Neoproterozoic island-arc terrane in a similar tectonic position to the Ar Rayn Terrane of Saudi Arabia (Whitehouse *et al.* 2001; Heikal *et al.* 2014; Yeshanew *et al.* 2015). Unfortunately no geochronological data are available for this terrane, but equivalent rocks in Somaliland (the Maydh Complex) yielded age constraints on basalts of 700–640 Ma (Sassi *et al.* 1993).

There are other basement inliers in Oman (Fig. 1), but the protoliths to the Jebel Ja'alan basement rocks are *c.* 50 Ma older than the oldest rock preserved in the Mirbat region of southern Oman (Fig. 1), which is the *c.* 835 Ma Sadh Gneiss complex (Rantakokko *et al.* 2014). Similar ages (*c.* 825–815 Ma) are also reported from the island of Socotra, which lay close to Mirbat before the opening of the Gulf of Aden (Denèle *et al.* 2013). The granodioritic basement found within Jebel Ja'alan (*c.* 840–830 Ma) is older than the granodioritic basement found in northern Huqf region (the Al-Jobah granite, 821–836 Ma; Bowring *et al.* 2007) and from volcanic rock clasts in Jebel Akhdar (Bowring *et al.* 2007). The age differences observed between basement inliers (Figs 16, 17) show a trend of basement becoming progressively younger westwards towards the Mirbat region, which was also suggested by Whitehouse, Pease & Al Khirbash (2016). This younging is interpreted to reflect the progressive accretion and migration of arc terranes during Tonian time. This interpreted direction of accretion is opposite to that for terranes in the eastern ANS (Johnson & Woldehaimanot, 2003; Johnson *et al.* 2011; Robinson *et al.* 2014; Robinson, Foden & Collins, 2015*a*), and would suggest that the Omani basement represents a tectonogeographic domain separate from that of the ANS.

In Gondwana Oman lay adjacent to NW India and, by Ediacaran times at least, a similar sedimentary package containing exceptional petroleum source rocks and evaporites was deposited across Rajasthan, Pakistan and through Oman (Cozzi, Rea & Craig, 2012). These packages were being deposited in a stable, passive margin environment (Allen, 2007) at the same time that rocks in the eastern Saudi Shield were forming at an active subduction margin (Cox *et al.* 2012). The pre-Ediacaran basement rocks in Rajasthan and Pakistan also share similarities with those of Oman. Granitoids have been dated from Rajasthan and from Nagar Parkar in eastern Sind (Pakistan) at *c.* 1100 Ma (Raza *et al.* 2012; Meert, Pandit & Kamenov, 2013). However, no evidence of pre-existing crust occurs west of the Western Margin Fault of the Aravalli–Delhi Orogen. Tonian granitoids and rhyolites occur in inliers through NW India and Pakistan, where they cluster into crystallization ages of *c.* 990–970 Ma (Haldar & Deb, 2001; Pandit *et al.* 2003), *c.* 860–820 Ma (Davies & Crawford, 1971; Deb *et al.* 2001; Van Lente *et al.* 2009; Just *et al.* 2011) and *c.* 775–760 Ma (Gregory *et al.* 2009; Van Lente *et al.* 2009; Ashwal *et al.* 2013; Meert, Pandit & Kamenov, 2013). The latter magmatic and extrusive phase forms one of the largest felsic igneous provinces on the planet, which is also traced to the Seychelles (Torsvik *et al.* 2001; Tucker, Ashwal & Torsvik, 2001), and may correlate with the northern Bemarivo Belt of Madagascar where the magmatism dates from *c.* 750–705 Ma (Collins, 2006; Thomas *et al.* 2009).

The NW margin of India is here interpreted as an extensive Stenian–Tonian (*c.* 1100–720 Ma) accretionary margin that extends as far as the Omani basement (Figs 16, 17). The rocks in Jebel Ja'alan form a critical part of this interpretation, linking Oman with the Indian subcontinent.

6. Conclusions

The basement of Jebel Ja'alan reveals a window into the accretionary margin of Neoproterozoic India during Tonian time. Pressure–temperature modelling indicates that the basement of Jebel Ja'alan reached peak conditions of *c.* 4–7.5 kbar at 650–700 °C. U–Pb data obtained from Al Wafi Schist monazite suggests that these peak metamorphic conditions occurred at 834 ± 12 Ma, with ^{40}Ar/^{39}Ar muscovite data suggesting rapid, exhumation-related cooling thereafter. The apparent thermal gradient calculated from the *P*–*T* modelling, in conjunction with trace-element geochemistry obtained from the Ja'alan Granite and Kamil Granodiorite, is used to interpret that the basement formed in a volcanic-arc environment. U–Pb zircon age data from igneous and meta-igneous lithologies in Jebel Ja'alan are indicative of magmatic activity during *c.* 890–830 Ma with subsequent emplacement of a dyke swarm consisting of three generations. Nd and Hf analyses of these same lithologies provide CHUR normalized values ranging from +0.56 to +6.78 and +2.3 to +13.3, respectively, suggesting a juvenile mantle origin with low crustal input or mixing with relatively young pre-existing crust. Depleted mantle model ages from Sm–Nd data show evolved Mesoproterozoic ages for the dyke swarm that became 'older' with progressively younger intrusions, suggesting that subduction-related contamination of the underlying lithospheric mantle during closure of the Mozambique Ocean.

Similarities can be drawn between the Omani basement and that of the ANS. *P*–*T* paths and related thermal gradients for terranes in Saudi Arabia and Egypt are comparable to those interpreted in this study, and timing of arc magmatism is similar for Jebel Ja'alan and the western arc terrane of Saudi Arabia. However, the geochronological data collected in this study suggests a progressive decrease in the ages of arc magmatism and metamorphism from NW India, through Jebel Ja'alan to the Huqf and Mirbat, implying arc accretion had occurred towards the modern-day west. Such a direction of accretion would indicate that Oman is not an eastwards extension of the ANS but is rather its own tectonic domain, related to NW India, Pakistan, the Seychelles and the Bemarivo Belt of north Madagascar.

Acknowledgements. This paper forms TRaX Record #366 and is a contribution to IGCP projects #628 (Gondwana Map) and #648 (Supercontinents and Global Dynamics). This project was funded by Australian Research Council Future Fellowship #FT120100340 to ASC. B. Wade and A. McFadden of Adelaide Microscopy are thanked for their help with collection of analytical data.

Supplementary material

To view supplementary material for this article, please visit https://doi.org/10.1017/S0016756817000061.

References

Abu-Alam, T., Hassan, M., Stüwe, K., Meyer, S. & Passchier, C. 2014. Multistage tectonism and metamorphism during Gondwana Collision: Baladiyah Complex, Saudi Arabia. *Journal of Petrology* **55**(10), 1941–64.

Abu El-Enen, M. M. 2011. Geochemistry, provenance, and metamorphic evolution of Gabal Samra Neoproterozoic metapelites, Sinai, Egypt. *Journal of African Earth Sciences* **59**(2–3), 269–82.

Allen, P. A. 2007. The Huqf Supergroup of Oman: basin development and context for Neoproterozoic glaciation. *Earth-Science Reviews* **84**(3), 139–85.

Allen, P. A., Leather, J. & Brasier, M. D. 2004. The Neoproterozoic Fiq glaciation and its aftermath, Huqf supergroup of Oman. *Basin Research* **16**(4), 507–34.

Allen, P. A., Leather, J., Brasier, M. D., Rieu, R., McCarron, M., le Guerroué, E., Etienne, J. L. & Cozzi, A. 2011. The Abu Mahara Group (Ghubrah and Fiq formations), Jabal Akhdar, Oman. In *The Geological Record of Neoproterozoic Glaciations* (eds E. Arnaud, G. P. Halverson & G. Shields), pp. 251–62. Geological Society of London, Memoir no. 36(1).

Allmendinger, R. W., Cardozo, N. & Fisher, D. M. 2011. *Structural Geology Algorithms: Vectors and Tensors*. Cambridge: Cambridge University Press.

Ashwal, L., Solanki, A., Pandit, M., Corfu, F., Hendriks, B., Burke, K. & Torsvik, T. 2013. Geochronology and geochemistry of Neoproterozoic Mt. Abu granitoids, NW India: regional correlation and implications for Rodinia paleogeography. *Precambrian Research* **236**, 265–81.

Baier, J., Audétat, A. & Keppler, H. 2008. The origin of the negative niobium tantalum anomaly in subduction zone magmas. *Earth and Planetary Science Letters* **267**(1–2), 290–300.

Bard, J. P. 1983. Metamorphism of an obducted island arc: example of the Kohistan sequence (Pakistan) in the Himalayan collided range. *Earth and Planetary Science Letters* **65**(1), 133–44.

Be'eri-Shlevin, Y., Eyal, M., Eyal, Y., Whitehouse, M. J. & Litvinovsky, B. 2012. The Sa'al volcano-sedimentary complex (Sinai, Egypt): a latest Mesoproterozoic volcanic arc in the northern Arabian Nubian Shield. *Geology* **40**(5), 403–6.

Blades, M. L., Collins, A. S., Foden, J., Payne, J. L., Xu, X., Alemu, T., Woldetinsae, G., Clark, C. & Taylor, R. J. 2015. Age and hafnium isotopic evolution of the Didesa and Kemashi domains, western Ethiopia. *Precambrian Research* **270**, 267–84.

Bowring, S. A., Grotzinger, J. P., Condon, D. J., Ramezani, J., Newall, M. J. & Allen, P. A. 2007. Geochronologic constraints on the chronostratigraphic framework of the Neoproterozoic Huqf Supergroup, Sultanate of Oman. *American Journal of Science* **307**(10), 1097–145.

Brown, M. 2007. Metamorphic conditions in orogenic belts: a record of secular change. *International Geology Review* **49**(3), 193–234.

Buick, I., Allen, C., Pandit, M., Rubatto, D. & Hermann, J. 2006. The Proterozoic magmatic and metamorphic history of the Banded Gneiss Complex, central Rajasthan, India: LA-ICP-MS U–Pb zircon constraints. *Precambrian Research* **151**(1), 119–42.

Cardozo, N. & Allmendinger, R. W. 2013. Spherical projections with OSXStereonet. *Computers & Geosciences* **51**, 193–205.

Collins, A. S. 2006. Madagascar and the amalgamation of Central Gondwana. *Gondwana Research* **9**(1), 3–16.

Collins, A. S. & Pisarevsky, S. A. 2005. Amalgamating eastern Gondwana: the evolution of the Circum-Indian Orogens. *Earth-Science Reviews* **71**(3), 229–70.

Corfu, F., Hanchar, J. M., Hoskin, P. W. & Kinny, P. 2003. Atlas of zircon textures. *Reviews in mineralogy and geochemistry* **53**(1), 469–500.

Corrie, S. L. & Kohn, M. J. 2008. Trace-element distributions in silicates during prograde metamorphic reactions: Implications for monazite formation. *Journal of Metamorphic Geology* **26**(4), 451–64.

Cox, G. M., Lewis, C. J., Collins, A. S., Halverson, G. P., Jourdan, F., Foden, J., Nettle, D. & Kattan, F. 2012. Ediacaran terrane accretion within the Arabian–Nubian Shield. *Gondwana Research* **21**(2), 341–52.

Cozzi, A., Rea, G. & Craig, J. 2012. From global geology to hydrocarbon exploration: Ediacaran-Early Cambrian petroleum plays of India, Pakistan and Oman. In *Geology and Hydrocarbon Potential of Neoproterozoic–Cambrian Basins in Asia* (eds G. M. Bhat, J. Craig, J. W. Thurrow, B. Thusu & A. Cozzi), pp, 131–62. Geological Society of London, Special Publication no. 366.

Davies, R. & Crawford, A. 1971. Petrography and age of the rocks of Bulland Hill, Kirana Hills, Sarghoda District, west Pakistan. *Geological Magazine* **108**(03), 235–46.

Davis, J. K., Meert, J. G. & Pandit, M. K. 2014. Paleomagnetic analysis of the Marwar Supergroup, Rajasthan, India and proposed interbasinal correlations. *Journal of Asian Earth Sciences* **91**, 339–51.

Deb, M., Thorpe, R., Krstic, D., Corfu, F. & Davis, D. 2001. Zircon U–Pb and galena Pb isotope evidence for an approximate 1.0 Ga terrane constituting the western margin of the Aravalli–Delhi orogenic belt, northwestern India. *Precambrian Research* **108**(3), 195–213.

Denèle, Y., Leroy, S., Pelleter, E., Pik, R., Talbot, J.-Y. & Khanbarri, K. 2013. The Cryogenian arc formation and successive high-K calc-alkaline plutons of Socotra Island (Yemen). In *Lithosphere Dynamics and Sedimentary Basins: The Arabian Plate and Analogues* (eds K. A. Hosani, F. Roure, R. Ellison & S. Lokier), pp. 335–60. Berlin, Heidelberg: Springer.

Dhuime, B., Hawkesworth, C. & Cawood, P. 2011. When continents formed. *Science* **331**(6014), 154–5.

Diener, J. & Powell, R. 2010. Influence of ferric iron on the stability of mineral assemblages. *Journal of Metamorphic Geology* **28**(6), 599–613.

Doebrich, J. L., Al-Jehani, A. M., Siddiqui, A. A., Hayes, T. S., Wooden, J. L. & Johnson, P. R. 2007. Geology and metallogeny of the Ar Rayn terrane, eastern Arabian shield: evolution of a Neoproterozoic continental-margin arc during assembly of Gondwana within the East African Orogen. *Precambrian Research* **158**(1), 17–50.

Elburg, M. & Foden, J. 1998. Temporal changes in arc magma geochemistry, northern Sulawesi, Indonesia. *Earth and Planetary Science Letters* **163**(1), 381–98.

Faryad, S. W., Collett, S., Finger, F., Sergeev, S. A., Čopjaková, R. & Siman, P. 2016. The Kabul Block (Afghanistan), a segment of the Columbia Supercontinent, with a Neoproterozoic metamorphic overprint. *Gondwana Research* **34**, 221–40.

Filbrandt, J., Nolan, S. & Ries, A. 1990. Late Cretaceous and early Tertiary evolution of Jebel Ja'alan and adjacent areas, NE Oman. In *The Geology and Tectonics of the Oman Region* (eds A. H. F. Robertson, M. P. Searle & A. C. Reis), pp. 697–714. Geological Society of London, Special Publication no. 49.

Fitton, J. & Gill, R. 1970. The oxidation of ferrous iron in rocks during mechanical grinding. *Geochimica et Cosmochimica Acta* **34**(4), 518–24.

Fritz, H., Dallmeyer, D. R., Wallbrecher, E., Loizenbauer, J., Hoinkes, G., Neumayr, P. & Khudeir, A. A. 2002. Neoproterozoic tectonothermal evolution of the Central Eastern Desert, Egypt: a slow velocity tectonic process of core complex exhumation. *Journal of African Earth Sciences* **34**(3–4), 137–55.

Gass, I., Ries, A., Shackleton, R. & Smewing, J. 1990. Tectonics, geochronology and geochemistry of the Precambrian rocks of Oman. In *The Geology and Tectonics of the Oman Region* (eds A. H. F. Robertson, M. P. Searle & A. C. Reis), pp. 585–99. Geological Society of London, Special Publication no. 49.

Goldstein, S., O'nions, R. & Hamilton, P. 1984. A Sm-Nd isotopic study of atmospheric dusts and particulates from major river systems. *Earth and Planetary Science Letters* **70**(2), 221–36.

Gregory, L. C., Meert, J. G., Bingen, B., Pandit, M. K. & Torsvik, T. H. 2009. Paleomagnetism and geochronology of the Malani Igneous Suite, Northwest India: implications for the configuration of Rodinia and the assembly of Gondwana. *Precambrian Research* **170**(1), 13–26.

Griffin, W., Wang, X., Jackson, S., Pearson, N., O'Reilly, S. Y., Xu, X. & Zhou, X. 2002. Zircon chemistry and magma mixing, SE China: in-situ analysis of Hf isotopes, Tonglu and Pingtan igneous complexes. *Lithos* **61**(3), 237–69.

HALDAR, S. & DEB, M. 2001. Geology and mineralization of Rajpura-Dariba lead-zinc belt, Rajasthan. In *Sediment-hosted Lead-Zink Deposit Modeling Program* (eds M. Deb & W. D. Goodfellow), pp. 177–87. New Delhi: Delhi-Udaipur, Elsevier.

HALVERSON, G. P., HURTGEN, M. T., PORTER, S. M. & COLLINS, A. S. 2009. Neoproterozoic-Cambrian biogeochemical evolution. *Developments in Precambrian Geology* **16**, 351–65.

HAMES, W. & BOWRING, S. 1994. An empirical evaluation of the argon diffusion geometry in muscovite. *Earth and Planetary Science Letters* **124**(1), 161–9.

HARRISON, T. M., CÉLÉRIER, J., AIKMAN, A. B., HERMANN, J. & HEIZLER, M. T. 2009. Diffusion of 40 Ar in muscovite. *Geochimica et Cosmochimica Acta* **73**(4), 1039–51.

HAWKESWORTH, C. & KEMP, A. 2006. Using hafnium and oxygen isotopes in zircons to unravel the record of crustal evolution. *Chemical Geology* **226**(3), 144–62.

HEIKAL, M. T. S., AL-KHIRBASH, S. A., HASSAN, A. M., AL-KOTBAH, A. M. & AL-SELWI, K. M. 2014. Lithostratigraphy, deformation history, and tectonic evolution of the basement rocks, Republic of Yemen: an overview. *Arabian Journal of Geosciences* **7**(5), 2007–18.

HODGES, K. 1991. Pressure-temperature paths. *Annual Review of Earth and Planetary Sciences* **19**, 207.

HOFFMAN, P. F., KAUFMAN, A. J., HALVERSON, G. P. & SCHRAG, D. P. 1998. A Neoproterozoic snowball earth. *Science* **281**(5381), 1342–6.

HOLLAND, T. & POWELL, R. 2011. An improved and extended internally consistent thermodynamic dataset for phases of petrological interest, involving a new equation of state for solids. *Journal of Metamorphic Geology* **29**(3), 333–83.

IMMENHAUSER, A., SCHREURS, G., GNOS, E., OTERDOOM, H. W. & HARTMANN, B. 2000. Late Palaeozoic to Neogene geodynamic evolution of the northeastern Oman margin. *Geological Magazine* **137**(1), 1–18.

JACKSON, S. E., PEARSON, N. J., GRIFFIN, W. L. & BELOUSOVA, E. A. 2004. The application of laser ablation-inductively coupled plasma-mass spectrometry to in situ U–Pb zircon geochronology. *Chemical Geology* **211**(1–2), 47–69.

JARRAR, G. H., THEYE, T., YASEEN, N., WHITEHOUSE, M., PEASE, V. & PASSCHIER, C. 2013. Geochemistry and P–T–t evolution of the Abu-Barqa Metamorphic Suite, SW Jordan, and implications for the tectonics of the northern Arabian–Nubian Shield. *Precambrian Research* **239**, 56–78.

JOHNSON, P., ANDRESEN, A., COLLINS, A., FOWLER, A., FRITZ, H., GHEBREAB, W., KUSKY, T. & STERN, R. 2011. Late Cryogenian–Ediacaran history of the Arabian–Nubian Shield: a review of depositional, plutonic, structural, and tectonic events in the closing stages of the northern East African Orogen. *Journal of African Earth Sciences* **61**(3), 167–232.

JOHNSON, P. R. & STEWART, I. C. 1995. Magnetically inferred basement structure in central Saudi Arabia. *Tectonophysics* **245**(1), 37–52.

JOHNSON, P. R. & WOLDEHAIMANOT, B. 2003. Development of the Arabian-Nubian Shield: perspectives on accretion and deformation in the northern East African Orogen and the assembly of Gondwana. In *Proterozoic East Gondwana: Supercontinent Assembly and Breakup* (eds M. Yoshida, B. E. Windley & S. Dasgupta), pp. 289–325. Geological Society of London, Special Publication no. 206.

JUST, J., SCHULZ, B., DE WALL, H., JOURDAN, F. & PANDIT, M. K. 2011. Monazite CHIME/EPMA dating of Erinpura granitoid deformation: Implications for Neoproterozoic tectono-thermal evolution of NW India. *Gondwana Research* **19**(2), 402–12.

KELSEY, D. E. & HAND, M. 2015. On ultrahigh temperature crustal metamorphism: Phase equilibria, trace element thermometry, bulk composition, heat sources, timescales and tectonic settings. *Geoscience Frontiers* **6**(3), 311–56.

KIL, Y. & JUNG, H. 2015. LA-ICP-MS analysis of natural rock samples using XRF glass beads. *Geosciences Journal* **19**(1), 45–52.

KORHONEN, F., POWELL, R. & STOUT, J. 2012. Stability of sapphirine+quartz in the oxidized rocks of the Wilson Lake terrane, Labrador: calculated equilibria in NCKFMASHTO. *Journal of Metamorphic Geology* **30**(1), 21–36.

KRÖNER, A. & STERN, R. J. 2004. Pan-African Orogeny. In *Encyclopedia of Geology* (eds R. C. Selley, R. M. Cocks & I. R. Plimer), pp. 1–12. Amsterdam: Elsevier.

LEATHER, J., ALLEN, P. A., BRASIER, M. D. & COZZI, A. 2002. Neoproterozoic snowball Earth under scrutiny: Evidence from the Fiq glaciation of Oman. *Geology* **30**(10), 891–4.

LI, Z.-X., BOGDANOVA, S., COLLINS, A., DAVIDSON, A., DE WAELE, B., ERNST, R., FITZSIMONS, I., FUCK, R., GLADKOCHUB, D. & JACOBS, J. 2008. Assembly, configuration, and break-up history of Rodinia: a synthesis. *Precambrian Research* **160**(1), 179–210.

MEERT, J. G. 2003. A synopsis of events related to the assembly of eastern Gondwana. *Tectonophysics* **362**(1), 1–40.

MEERT, J. G. & LIEBERMAN, B. S. 2008. The Neoproterozoic assembly of Gondwana and its relationship to the Ediacaran–Cambrian radiation. *Gondwana Research* **14**(1), 5–21.

MEERT, J. G., PANDIT, M. K. & KAMENOV, G. D. 2013. Further geochronological and paleomagnetic constraints on Malani (and pre-Malani) magmatism in NW India. *Tectonophysics* **608**, 1254–67.

MERCOLLI, I., BRINER, A. P., FREI, R., SCHÖNBERG, R., NÄGLER, T. F., KRAMERS, J. & PETERS, T. 2006. Lithostratigraphy and geochronology of the Neoproterozoic crystalline basement of Salalah, Dhofar, Sultanate of Oman. *Precambrian Research* **145**(3), 182–206.

MERDITH, A., MULLER, D., COLLINS, A., WILLIAMS, S., PISAREVSKY, S., FODEN, J., ARCHIBALD, D., BLADES, M. L., ALESSIO, B., ARMISTEAD, S., PLAVSA, D. & CLARK, C. In press. A full-plate global reconstruction of the Neoproterozoic. *Gondwana Research*.

MILLER, D. M., GOLDSTEIN, S. L. & LANGMUIR, C. H. 1994. Cerium/lead and lead isotope ratios in arc magmas and the enrichment of lead in the continents. *Nature* **368**(6471), 514–20.

MORRISSEY, L. J., HAND, M. & KELSEY, D. E. 2015. Multi-stage metamorphism in the Rayner–Eastern Ghats Terrane: P–T–t constraints from the northern Prince Charles Mountains, east Antarctica. *Precambrian Research* **267**, 137–63.

PALLISTER, J. S., COLE, J. C., STOESER, D. B. & QUICK, J. E. 1990. Use and abuse of crustal accretion calculations. *Geology* **18**(1), 35–9.

PANDEY, B., GUPTA, J., SARMA, K. & SASTRY, C. 1997. Sm-Nd, Pb-Pb and Rb-Sr geochronology and petrogenesis of the mafic dyke swarm of Mahbubnagar, South India: implications for Paleoproterozoic crustal evolution of the Eastern Dharwar Craton. *Precambrian Research* **84**(3), 181–96.

Pandit, M., Carter, L., Ashwal, L., Tucker, R., Torsvik, T., Jamtveit, B. & Bhushan, S. 2003. Age, petrogenesis and significance of 1Ga granitoids and related rocks from the Sendra area, Aravalli Craton, NW India. *Journal of Asian Earth Sciences* **22**(4), 363–81.

Payne, J., Hand, M., Barovich, K. & Wade, B. 2008. Temporal constraints on the timing of high-grade metamorphism in the northern Gawler Craton: implications for assembly of the Australian Proterozoic. *Australian Journal of Earth Sciences* **55**(5), 623–40.

Payne, J. L., McInerney, D. J., Barovich, K. M., Kirkland, C. L., Pearson, N. J. & Hand, M. 2016. Strengths and limitations of zircon Lu-Hf and O isotopes in modelling crustal growth. *Lithos* **248**, 175–92.

Payne, J. L., Pearson, N. J., Grant, K. J. & Halverson, G. P. 2013. Reassessment of relative oxide formation rates and molecular interferences on in situ lutetium–hafnium analysis with laser ablation MC-ICP-MS. *Journal of Analytical Atomic Spectrometry* **28**(7), 1068–79.

Powell, R., White, R., Green, E., Holland, T. & Diener, J. 2014. On parameterizing thermodynamic descriptions of minerals for petrological calculations. *Journal of Metamorphic Geology* **32**(3), 245–60.

Rantakokko, N. E., Whitehouse, M. J., Pease, V. & Windley, B. F. 2014. Neoproterozoic evolution of the eastern Arabian basement based on a refined geochronology of the Marbat region, Sultanate of Oman. In *Tectonic Evolution of the Oman Mountains* (eds H. R. Rollinson, M. P. Searle, I. A. Abbasi, A. I. Al-Lazki & M. H. Al Kindi), pp. 107–27. Geological Society of London, Special Publication no. 392.

Raza, M., Khan, A., Bhardwaj, V. & Rais, S. 2012. Geochemistry of Mesoproterozoic sedimentary rocks of upper Vindhyan Group, southeastern Rajasthan and implications for weathering history, composition and tectonic setting of continental crust in the northern part of Indian shield. *Journal of Asian Earth Sciences* **48**, 160–72.

Renne, P. R., Balco, G., Ludwig, K. R., Mundil, R. & Min, K. 2011. Response to the comment by WH Schwarz *et al.* on "Joint determination of 40 K decay constants and 40 Ar∗/40 K for the Fish Canyon sanidine standard, and improved accuracy for 40 Ar/39 Ar geochronology" by PR Renne et al. (2010). *Geochimica et Cosmochimica Acta* **75**(17), 5097–100.

Rieu, R., Allen, P. A., Cozzi, A., Kosler, J. & Bussy, F. 2007. A composite stratigraphy for the Neoproterozoic Huqf Supergroup of Oman: integrating new litho-, chemo- and chronostratigraphic data of the Mirbat area, southern Oman. *Journal of the Geological Society* **164**(5), 997–1009.

Robinson, F., Foden, J. & Collins, A. 2015a. Geochemical and isotopic constraints on island arc, synorogenic, post-orogenic and anorogenic granitoids in the Arabian Shield, Saudi Arabia. *Lithos* **220**, 97–115.

Robinson, F., Foden, J. & Collins, A. 2015*b*. Zircon geochemical and geochronological constraints on contaminated and Enriched Mantle sources beneath the Arabian Shield, Saudi Arabia. *The Journal of Geology* **123**(5), 463–89.

Robinson, F., Foden, J., Collins, A. & Payne, J. 2014. Arabian Shield magmatic cycles and their relationship with Gondwana assembly: insights from zircon U–Pb and Hf isotopes. *Earth and Planetary Science Letters* **408**, 207–25.

Roger, J., Bechennec, F., Janjou, D., Le Metour, J., Wyns, R. & Beurrier, M. 1991. Geological Map of Ja'alan, Sheet NF 40–8 E, 1–100 000. Directorate General of Minerals, Oman Ministry of Petroleum and Minerals.

Sassi, F., Visona, D., Ferrara, G., Gatto, G., Ibrahim, H., Said, A. & Tonarini, S. 1993. The crystalline basement of Northern Somalia: lithostratigraphy and sequence of events. In *Geology and Mineral Resources of Somalia and Surrounding Regions* (eds E. Abbate, M. Sagri & F. Sassi), pp. 3–40. 1st Agron Oltemare, Firenze, Relaz. Monogr. 113.

Sláma, J., Košler, J., Condon, D. J., Crowley, J. L., Gerdes, A., Hanchar, J. M., Horstwood, M. S., Morris, G. A., Nasdala, L. & Norberg, N. 2008. Plešovice zircon—a new natural reference material for U–Pb and Hf isotopic microanalysis. *Chemical Geology* **249**(1), 1–35.

Smith, H. A. & Barreiro, B. 1990. Monazite U-Pb dating of staurolite grade metamorphism in pelitic schists. *Contributions to Mineralogy and Petrology* **105**(5), 602–15.

Stern, R. J. 1994. Arc-assembly and continental collision in the Neoproterozoic African orogen: implications for the consolidation of Gondwanaland. *Annual Review of Earth and Planetary Sciences* **22**, 319–51.

Stern, R. J. & Johnson, P. 2010. Continental lithosphere of the Arabian Plate: a geologic, petrologic, and geophysical synthesis. *Earth-Science Reviews* **101**(1), 29–67.

Stüwe, K. 2007. *Geodynamics of the Lithosphere: An Introduction*. Berlin, Heidelberg: Springer Science & Business Media.

Sun, S.-S. & McDonough, W. 1989. Chemical and isotopic systematics of oceanic basalts: implications for mantle composition and processes. In *Magmatism in the Ocean Basins* (eds A. D. Saunders & M. J. Norry), pp. 313–45. Geological Society of London, Special Publication no. 42.

Thomas, R. J., De Waele, B., Schofield, D., Goodenough, K. M., Horstwood, M., Tucker, R., Bauer, W., Annells, R., Howard, K. & Walsh, G. 2009. Geological evolution of the Neoproterozoic Bemarivo Belt, northern Madagascar. *Precambrian Research* **172**(3), 279–300.

Torsvik, T., Carter, L., Ashwal, L., Bhushan, S., Pandit, M. & Jamtveit, B. 2001. Rodinia refined or obscured: palaeomagnetism of the Malani igneous suite (NW India). *Precambrian Research* **108**(3), 319–33.

Tuccillo, M., Essene, E. & Van Der Pluijm, B. 1990. Growth and retrograde zoning in garnets from high-grade, metapelites: Implications for pressure-temperature paths. *Geology* **18**(9), 839–42.

Tucker, R., Ashwal, L. & Torsvik, T. 2001. U–Pb geochronology of Seychelles granitoids: a Neoproterozoic continental arc fragment. *Earth and Planetary Science Letters* **187**(1), 27–38.

Van Lente, B., Ashwal, L., Pandit, M., Bowring, S. & Torsvik, T. 2009. Neoproterozoic hydrothermally altered basaltic rocks from Rajasthan, northwest India: implications for late Precambrian tectonic evolution of the Aravalli Craton. *Precambrian Research* **170**(3), 202–22.

Wade, B., Hand, M., Maidment, D., Close, D. & Scrimgeour, I. 2008. Origin of metasedimentary and igneous rocks from the Entia Dome, eastern Arunta region, central Australia: a U–Pb LA-ICPMS, SHRIMP and Sm–Nd isotope study. *Australian Journal of Earth Sciences* **55**(5), 703–19.

WENDT, I. & CARL, C. 1991. The statistical distribution of the mean squared weighted deviation. *Chemical Geology: Isotope Geoscience Section* **86**(4), 275–85.

WESTERHOF, A. B., HÄRMÄ, P., ISABIRYE, E., KATTO, E., KOISTINEN, T., KUOSMANEN, E., LEHTO, T., LEHTONEN, M. I., MÄKITIE, H. & MANNINEN, T. 2014. *Geology and Geodynamic Development of Uganda with Explanation of the 1: 1,000,000 Scale Geological Map*. Espoo, Finland: Geological Survey of Finland.

WHITE, R., POWELL, R., HOLLAND, T., JOHNSON, T. & GREEN, E. 2014. New mineral activity–composition relations for thermodynamic calculations in metapelitic systems. *Journal of Metamorphic Geology* **32**(3), 261–86.

WHITE, R., POWELL, R. & JOHNSON, T. 2014. The effect of Mn on mineral stability in metapelites revisited: new a–x relations for manganese-bearing minerals. *Journal of Metamorphic Geology* **32**(8), 809–28.

WHITEHOUSE, M., PEASE, V. & AL KHIRBASH, S. 2016. Neoproterozoic crustal growth at the margin of the East Gondwana continent - age and isotopic constraints from the easternmost inliers of Oman. *International Geology Review* **58**(14), 2046–64.

WHITEHOUSE, M. J., WINDLEY, B. F., STOESER, D. B., AL-KHIRBASH, S., BA-BTTAT, M. A. & HAIDER, A. 2001. Precambrian basement character of Yemen and correlations with Saudi Arabia and Somalia. *Precambrian Research* **105**(2), 357–69.

WING, B. A., FERRY, J. M. & HARRISON, T. M. 2003. Prograde destruction and formation of monazite and allanite during contact and regional metamorphism of pelites: petrology and geochronology. *Contributions to Mineralogy and Petrology* **145**(2), 228–50.

WOODHEAD, J., HERGT, J., SHELLEY, M., EGGINS, S. & KEMP, R. 2004. Zircon Hf-isotope analysis with an excimer laser, depth profiling, ablation of complex geometries, and concomitant age estimation. *Chemical Geology* **209**(1), 121–35.

WORTHING, M. 2005. Petrology and geochronology of a Neoproterozoic dyke swarm from Marbat, South Oman. *Journal of African Earth Sciences* **41**(3), 248–65.

YESHANEW, F. G., PEASE, V., WHITEHOUSE, M. J. & AL-KHIRBASH, S. 2015. Zircon U–Pb geochronology and Nd isotope systematics of the Abas terrane, Yemen: implications for Neoproterozoic crust reworking events. *Precambrian Research* **267**, 106–20.

ZHAO, G., WILDE, S. A., CAWOOD, P. A. & SUN, M. 2001. Archean blocks and their boundaries in the North China Craton: lithological, geochemical, structural and P–T path constraints and tectonic evolution. *Precambrian Research* **107**(1), 45–73.